Radar Retrieval Evaluation and Investigation of Dendritic Growth Layer Polarimetric Signatures in a Winter Storm

EDWIN L. DUNNAVAN,[a,b] JACOB T. CARLIN,[a,b] JIAXI HU,[a,b] PETAR BUKOVČIĆ,[a,b] ALEXANDER V. RYZHKOV,[a,b] GREG M. MCFARQUHAR,[a,c] JOSEPH A. FINLON,[d] SERGEY Y. MATROSOV,[e,f] AND DAVID J. DELENE[g]

[a] *Cooperative Institute for Severe and High-Impact Weather Research and Operations, Norman, Oklahoma*
[b] *NOAA/OAR National Severe Storms Laboratory, Norman, Oklahoma*
[c] *School of Meteorology, University of Oklahoma, Norman, Oklahoma*
[d] *Department of Atmospheric Sciences, University of Washington, Seattle, Washington*
[e] *Cooperative Institute for Research in Environmental Sciences, University of Colorado Boulder, Boulder, Colorado*
[f] *Physical Sciences Laboratory, NOAA, Boulder, Colorado*
[g] *Department of Atmospheric Sciences, University of North Dakota, Grand Forks, North Dakota*

(Manuscript received 19 October 2021, in final form 29 June 2022)

ABSTRACT: This study evaluates ice particle size distribution and aspect ratio φ Multi-Radar Multi-Sensor (MRMS) dual-polarization radar retrievals through a direct comparison with two legs of observational aircraft data obtained during a winter storm case from the Investigation of Microphysics and Precipitation for Atlantic Coast-Threatening Snowstorms (IMPACTS) campaign. In situ cloud probes, satellite, and MRMS observations illustrate that the often-observed K_{dp} and Z_{DR} enhancement regions in the dendritic growth layer can either indicate a local number concentration increase of dry ice particles or the presence of ice particles mixed with a significant number of supercooled liquid droplets. Relative to in situ measurements, MRMS retrievals on average underestimated mean volume diameters by 50% and overestimated number concentrations by over 100%. IWC retrievals using Z_{DR} and K_{dp} within the dendritic growth layer were minimally biased relative to in situ calculations where retrievals yielded -2% median relative error for the entire aircraft leg. Incorporating φ retrievals decreased both the magnitude and spread of polarimetric retrievals below the dendritic growth layer. While φ radar retrievals suggest that observed dendritic growth layer particles were nonspherical ($0.1 \le \varphi \le 0.2$), in situ projected aspect ratios, idealized numerical simulations, and habit classifications from cloud probe images suggest that the population mean φ was generally much higher. Coordinated aircraft radar reflectivity with in situ observations suggests that the MRMS systematically underestimated reflectivity and could not resolve local peaks in mean volume diameter sizes. These results highlight the need to consider particle assumptions and radar limitations when performing retrievals.

SIGNIFICANCE STATEMENT: Developing snow is often detectable using weather radars. Meteorologists combine these radar measurements with mathematical equations to study how snow forms in order to determine how much snow will fall. This study evaluates current methods for estimating the total number and mass, sizes, and shapes of snowflakes from radar using images of individual snowflakes taken during two aircraft legs. Radar estimates of snowflake properties were most consistent with aircraft data inside regions with prominent radar signatures. However, radar estimates of snowflake shapes were not consistent with observed shapes estimated from the snowflake images. Although additional research is needed, these results bolster understanding of snow-growth physics and uncertainties between radar measurements and snow production that can improve future snowfall forecasting.

KEYWORDS: Atmosphere; Clouds; Snowfall; Stratiform clouds; In situ atmospheric observations; Radars/radar observations

1. Introduction

Dual-polarization radar provides a unique set of variables that can be used to infer winter cloud and precipitation characteristics. A better understanding of such characteristics is essential for accurate snow forecasting (Reeves et al. 2014) and hydrometeor classification (Thompson et al. 2014). The recent advent of ubiquitous dual-polarization capabilities in operational NEXRAD instruments provides ample opportunity for developing appropriate methods to exploit these polarimetric capabilities. As a result, operational radars can help to improve snowfall forecasting capabilities and further enhance understanding of the microphysical particle properties and processes that cause dual-polarization signatures or "fingerprints" (Kumjian et al. 2016).

To complement the recent polarimetric advances in radar meteorology, newer studies have developed mathematical theories and methodologies that exploit multiple radar variables to retrieve parameters describing particle size distributions (PSDs; Ryzhkov and Zrnić 2019), particle characteristics such as shape and orientation (e.g., Melnikov and Straka 2013; Matrosov et al. 2017; Matrosov 2020; Matrosov et al. 2020), ice water content (IWC; Ryzhkov et al. 1998), and snow precipitation rates (S; Bukovčić et al. 2018, 2020). These microphysical retrievals are either purely empirical, thereby linking radar quantities directly to IWC or S through the use of (bivariate) power laws (e.g., Hogan et al. 2006; Bukovčić et al. 2018; Nguyen et al. 2019; Bukovčić et al. 2020), or estimated from PSD parameters

---

Corresponding author: Edwin L. Dunnavan, edwin.dunnavan@noaa.gov

DOI: 10.1175/JAMC-D-21-0220.1

that, in turn, are used to calculate IWC or S (e.g., Ryzhkov and Zrnić 2019). Microphysical relations that rely on PSD characterization must make numerous approximations and assumptions about the shapes, densities, orientations, and degree of riming for all particles (see Ryzhkov and Zrnić 2019). Such assumptions are very crude since ice particles are well known to exhibit a wide variety of microphysical characteristics even within the same ice particle class (Locatelli and Hobbs 1974; Mitchell 1996) and are expected to vary spatiotemporally depending upon environmental conditions (Bailey and Hallett 2009) and growth histories (Chen and Lamb 1994; Harrington et al. 2013; Sulia et al. 2013; Jensen and Harrington 2015). Despite this variability, current radar retrieval techniques often employ the same set of assumptions and approximations including a fixed (oblate) spheroid particle shape, a fixed density–size (ρ_s–D) relation, and a fixed canting angle standard deviation σ. Such assumptions necessitate their own sets of errors and uncertainties (Westbrook 2014; Schrom and Kumjian 2018), yet these assumptions have not yet been rigorously evaluated through careful analyses with in situ cloud probe observations.

Radar retrievals using reflectivity Z, differential reflectivity $Z_{\rm DR}$, specific differential phase $K_{\rm dp}$, and copolar correlation coefficient $\rho_{\rm hv}$ should theoretically be most accurate in regions where all four variables are most prominent.[1] One such scenario can regularly occur within the dendritic growth layer, approximately from $-12°$ to $-18°$C, where $Z_{\rm DR}$ and $K_{\rm dp}$ are elevated ($0.5 < Z_{\rm DR} < 5.0$ dB and $0.2 < K_{\rm dp} < 0.8°\ {\rm km}^{-1}$ at S band) and $\rho_{\rm hv}$ is diminished ($0.96 < \rho_{\rm hv} < 0.99$). For Rayleigh scattering, $K_{\rm dp}$ depends upon the inverse of radar wavelength. As such, dendritic growth layer $K_{\rm dp}$ enhancements are roughly 3 times as high for X band as for S band. Enhanced $Z_{\rm DR}$ and $K_{\rm dp}$ implies the presence of anisotropic particles such as dendrites or hexagonal plates where the magnitude of $Z_{\rm DR}$ and $K_{\rm dp}$ depends upon the particle aspect ratios and densities. In addition, unlike $Z_{\rm DR}$, which is not sensitive to number concentration, $K_{\rm dp}$ is dependent upon number concentration and can therefore indicate enhancements in the number of particles as well. Diminished $\rho_{\rm hv}$ suggests a diversity of different particle types, shapes, densities, and/or orientations. Many studies have investigated these dendritic growth layer signatures and have provided various theories that explain the underlying microphysical causes (Ryzhkov and Zrnić 1998; Kennedy and Rutledge 2011; Andrić et al. 2013; Bechini et al. 2013; Grazioli et al. 2015; Moisseev et al. 2015; Schrom et al. 2015; Schrom and Kumjian 2016, 2018; Kumjian and Lombardo 2017; Griffin et al. 2018) yet there is no overall consensus for the validity or reconciliation of these theories. Some studies such as Kennedy and Rutledge (2011), Schrom et al. (2015), and Schrom and Kumjian (2018) have hypothesized that the $K_{\rm dp}$ and $Z_{\rm DR}$ dendritic growth layer enhancements result from large dendrites that grow in situ, whereas other studies have hypothesized the role of "seeder–feeder"-type processes and oblate aggregates as a potential explanation (Moisseev et al. 2015). Furthermore, other studies such as Griffin et al. (2018) have provided evidence that hexagonal plates in the dendritic growth layer can cause extremely large values of $Z_{\rm DR}$, and they attributed $Z_{\rm DR}$ and $K_{\rm dp}$ enhancements to separate types of particles. Still other studies such as Andrić et al. (2013) and Sinclair et al. (2016) attribute $K_{\rm dp}$ enhancements to secondary ice production of small, anisotropic crystals. Homogeneous oblate spheroids are often used in these studies to represent various ice particle habits; however, recent discrete dipole approximation modeling results (Westbrook 2014; Schrom and Kumjian 2018) illustrate that this approximation can severely underestimate or overestimate both $Z_{\rm DR}$ and $K_{\rm dp}$ for branched planar crystals depending upon the assumed effective density.

Untangling the various causes of these polarimetric signatures requires careful consideration of collocated radar and in situ observations along with appropriate, physical approximations that govern each retrieval. However, few studies have directly compared dual-polarization radar retrieval estimates with in situ observations (e.g., Ryzhkov et al. 1998; Nguyen et al. 2019; Murphy et al. 2020). Such comparison efforts are essential to ensure retrievals are consistent with observations and to investigate any biases and uncertainties in such calculations. Indeed, each retrieval relies on physical assumptions about ice particle shapes, densities, orientations, and degree of riming that not only influence the PSD parameters but the resulting quantities (e.g., IWC or S) that often follow from such assumptions through weighted integration of the retrieved PSD. Any errors in radar quantities from, for instance, calibration biases or spatiotemporal matching will necessarily propagate into any retrieved quantity; it is our understanding that few studies have actually quantified how radar variable uncertainties would affect retrievals and how the magnitude of such uncertainties compare to the retrieved quantities themselves.

Toward this end, this paper evaluates current PSD and aspect ratio retrieval methodologies through direct comparison of Multi-Radar Multi-Sensor (MRMS; Zhang et al. 2016) observations collocated with in situ aircraft observations obtained during the 2020 Investigation of Microphysics and Precipitation for Atlantic Coast-Threatening Storms (IMPACTS; McMurdie et al. 2022) campaign. While we only evaluate two flight legs of this winter storm case (constituting approximately 1 h of flight data), the MRMS in situ collocation approach and subsequent investigation into fascinating polarimetric signatures can be thought of as a first attempt at understanding such radar features through the combined use of multiple observational platforms. This study is the first to incorporate polarimetric MRMS data and MRMS uncertainties in the use of radar retrieval algorithms and the first to attempt collocation of MRMS observations with measurements obtained from in situ aircraft data.

2. The MRMS system

In this study, the MRMS mosaic of NEXRAD WSR-88D instruments is used to collocate ice microphysical radar retrievals with in situ aircraft measurements. The MRMS is an attractive system for these tasks because the system incorporates data from multiple radars. Thus, the use of multiple radars allows for a much larger spatial range than provided by a single radar and can help mitigate potential calibration biases introduced by individual radars. The MRMS is also an operational product.

---

[1] Herein, radar variable subscripts represent either linear units (lowercase) or logarithmic units (uppercase).

Therefore, it would be possible for future MRMS upgrades to include real-time CONUS-wide microphysical retrieval estimates.

The MRMS consists of 143 WSR-88Ds as well as 30 radars from Environment and Climate Change Canada seamlessly interpolated onto a common 3D CONUS grid, forming a mosaic. Each individual WSR-88D typically has 0.5° (azimuthal) by 250-m (range) resolution with ranges of 420 km at each site. However, the MRMS grid itself has a horizontal resolution of 0.01° latitude × 0.01° longitude that corresponds to about a 1.1-km resolution and 33 irregularly spaced vertical levels with 250-m resolution from 0 to 3 km MSL, 500-m resolution from 3 to 9 km MSL, and 1000-m resolution from 9 to 20 km MSL (Smith et al. 2016). This grid in general has a temporal resolution of 2 min for Z and 10 min for each polarimetric variable. However, to maintain consistent radar retrievals (which use both Z and each polarimetric variable), we use the 10-min MRMS data. The MRMS radar merging methodology comes from the work of Lakshmanan et al. (2006) who uses exponential weights in time and in distance between the individual radar data bin and the MRMS grid cell. Radar data are averaged only between radars, whereas MRMS grid points near each radar are not smoothed. The K_{dp} is calculated by using a local linear fitting to differential phase along the radial direction (Ryzhkov and Zrnić 1996).

MRMS uncertainties for spatiotemporal collocation with aircraft can result from a number of factors. For example, individual radars can be miscalibrated, which can affect Z and Z_{DR}, and K_{dp} can be noisy. MRMS uncertainties can also result from the multiradar merging algorithm (Lakshmanan et al. 2006), which preferentially weights data according to time and distance. Therefore, while there are many sources of potential error from the MRMS, we develop a methodology for incorporating some of these errors in section 4a when we perform our radar retrievals.

3. Case description

In situ and radar observations used in this work are from the 7 February 2020 IMPACTS case. Measurements were made across the final frontal system in a series of shortwaves that moved across the Ohio Valley and mid-Atlantic region in the preceding days. The fast-moving shortwave associated with the surface low pressure system was embedded in an extremely deep and negatively tilted trough centered over the Mississippi Valley with an attendant jet streak at 300 hPa off the mid-Atlantic coast that exceeded 225 kt (116 m s^{-1}) by 0000 UTC 8 February 2020.

At the surface, a low pressure system formed in the Tennessee Valley at 1200 UTC 6 February 2020 and moved quickly northeast, undergoing rapid cyclogenesis on 7 February 2020 and deepening to 966 hPa by 0000 UTC 8 February 2020. Concurrently, an Arctic front moved southward on the backside of the system, resulting in frontogenetic forcing within the deformation zone over the Hudson Valley. A broad swath of heavy snow fell across the interior Northeast and New England, with up to 30 cm of snow falling across parts of central New York and snowfall rates exceeding 3–5 cm h^{-1}.

The NASA P3 aircraft flew from 1400 to 1900 UTC, making multiple passes cutting across the cold front situated in upstate New York (Fig. 1). Another aircraft, the NASA ER2, made coordinated passes with the P3 for some of these flight legs as well. The ER2 aircraft flew above the P3 aircraft at approximately 20 km MSL and utilized multiple radar and lidar instruments. In particular, the ER2 aircraft housed a nadir-pointing X-band radar (EXRAD) as well as Ku-band and Ka-band radars (HIWRAP) that could be used to collocate radar reflectivity with the P3 aircraft location.

The west side of the frontal boundary was composed of snow at the surface while the east side of the frontal boundary was composed of rain at the surface. Herein, we focus on performing radar and in situ retrievals along the first two P3 legs, which correspond to time periods when the P3 was to the west of the frontal boundary (Fig. 1). Leg 1 corresponds to roughly 1508–1524 UTC when the P3 flew west to east, whereas leg 2 corresponds to roughly 1530–1551 UTC when the P3 flew east to west. During leg 1, the P3 aircraft flew at approximately 5 km MSL ($T \approx -16$°C) throughout the flight leg, whereas in leg 2 the P3 aircraft flew at approximately 3.5 km MSL but with temperatures decreasing from approximately −6°C at 1530 UTC to −13°C at 1551 UTC (Figs. 1d,e).

Figure 2 shows a Cartesian representation of the 5-km MRMS horizontal cross section for Z, Z_{DR}, and K_{dp} at 1510 and 1520 UTC during leg 1 along with the P3 locations for these times. At both time periods, there are two separate K_{dp} and Z_{DR} enhancement regions. At each period, the P3 aircraft is in the vicinity of K_{dp} values over 0.2° km^{-1} and Z_{DR} values over 1.0 dB. In comparison with the stratiform nature of Z, these enhancement regions are very small [O(10 km)]. Despite these features occurring on such a small scale, the P3 aircraft flew through both regions nearly 100 km apart. This implies that it is possible for us to utilize in situ measurements taken aboard the aircraft in conjunction with the MRMS to directly investigate the microphysical properties of these regions (and in between) and to connect these dual-polarization radar features with *physical*, causal explanations. It is important to realize that the small scale of these features shown in Fig. 2 and the even smaller scale sampling volumes swept out by the in situ measurement probes provide a host of uncertainties in such an investigation. As a result, the next section lays out a general methodology for collocating the MRMS with the P3 in situ measurements that encompasses these spatiotemporal uncertainties.

4. Methodology

a. In situ aircraft and MRMS radar collocation

Unlike other studies that have used nearest-neighbor, interpolation, or averaging approaches for collocation (Nguyen et al. 2019; Murphy et al. 2020; Chase et al. 2021), collocation of aircraft and MRMS radar data for this study is performed through a bootstrapping approach whereby the MRMS grid points closest to the P3 aircraft are resampled (i.e., sampled with replacement) to impute P3 radar retrieval statistics (e.g., mean and covariance). To do this, we use the latitude, longitude and MSL altitude for each P3 time stamp and calculate the total horizontal distances to each MRMS grid point. Only MRMS horizontal grid points less than 1 km away from the P3 are used

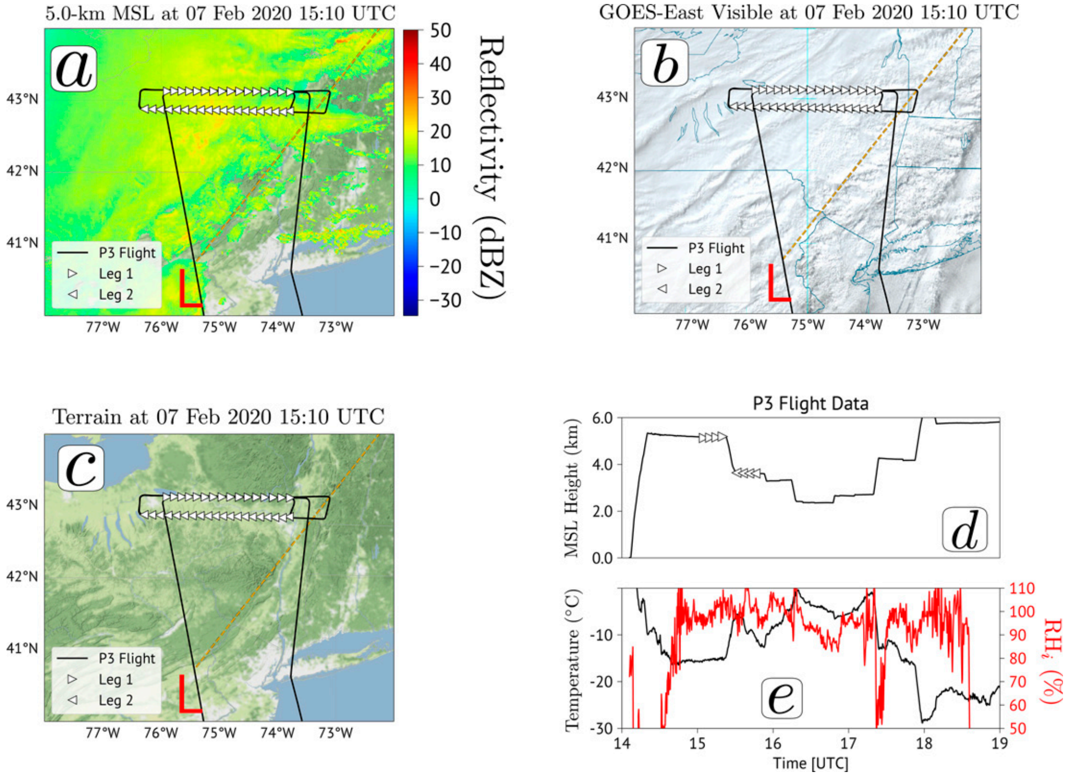

FIG. 1. (a) 5.0-km Z at 1510 UTC 7 Feb 2020 from the MRMS system at 5.0 km MSL. The orange, dashed line corresponds to a convergence line estimate adapted from the 1500 UTC 7 Feb 2020 Weather Prediction Center surface analysis. The P3 flight track is shown in black, with the flight direction of each of the relevant flight legs denoted with arrows. (b) As in (a), but with the GOES-East visible satellite. (c) As in (a) and (b), but with just the terrain overlay. Also shown are time series of (d) altitude and (e) temperature (black; °C) with relative humidity with respect to ice (red; %) measured by the P3 probes. The periods corresponding to each leg are additionally shown as white triangles in (a)–(c).

for retrievals. We then estimate retrievals by weighting the sampled retrievals along the horizontal,

$$w_{\mathrm{MRMS/P3}} = \frac{1}{\sqrt{(x_{\mathrm{MRMS}} - x_{\mathrm{P3}})^2 + (y_{\mathrm{MRMS}} - y_{\mathrm{P3}})^2 + (v_{t,\mathrm{P3}}\Delta t_{\mathrm{MRMS/P3}})^2}}, \tag{1}$$

and along the vertical,

$$w_{z,\mathrm{MRMS/P3}} = \frac{1}{\sqrt{(z_{\mathrm{MRMS}} - z_{\mathrm{P3}})^2}}, \tag{2}$$

where $v_{t,\mathrm{P3}}$ is the P3 aircraft ground speed in meters per second, $\Delta t_{\mathrm{MRMS/P3}}$ is the time difference between the P3 time stamp and the MRMS time stamp, and (x, y, z) represents the Cartesian locations of the MRMS grid points and the P3 aircraft. Figure 3 shows an example of the horizontal bootstrapping procedure for a time period (1513 UTC) between neighboring MRMS time stamps (1510 and 1520 UTC). For each P3 time period, we calculate the horizontal distance between the P3 location and each MRMS grid point. Only MRMS grid points less than 1 km from the P3 are included in the collocated statistics as indicated by the gray circles in Fig. 3. The temporal term in Eq. (1) can be thought of as the distance (red lines in Fig. 3) that the P3 travels between a MRMS time stamp, for which there are no temporal errors, and a time period in between each MRMS time stamp. This means that MRMS gridpoint locations that are spatially and temporally closer to the P3 aircraft at each P3 time stamp are preferentially drawn. We resample sets of x_{MRMS}, y_{MRMS}, and t_{MRMS} grid points 10 000 times with replacement for each P3 time period. We then perform the same bootstrap sampling but with only the vertical weighting [Eq. (2)] to determine which height levels are drawn for each of the 10 000 samples.

We then use each sampled set of MRMS radar variables to retrieve three key bulk ice microphysical quantities: mean volume diameter D_m, number concentration N_t, and IWC. The D_m for this work is defined as the ratio of the fourth and third moments of the equivolume size distribution.

b. In situ probes and data processing methodologies

The P3 aircraft housed several different cloud probe instruments including a two-dimensional stereo (2DS) that has both horizontal (2DS-H) and vertical (2DS-V) oriented photodiode arrays, two high-volume precipitation spectrometers (HVPS-A and HVPS-B), a cloud probe imager (CPI), a fast-cloud droplet probe (FCDP), and a Rosemount icing detector (RICE), as well as several other probes not used in this study (Delene 2022). Aircraft probe data were processed using the Airborne Data Processing and Analysis package (Delene 2011).

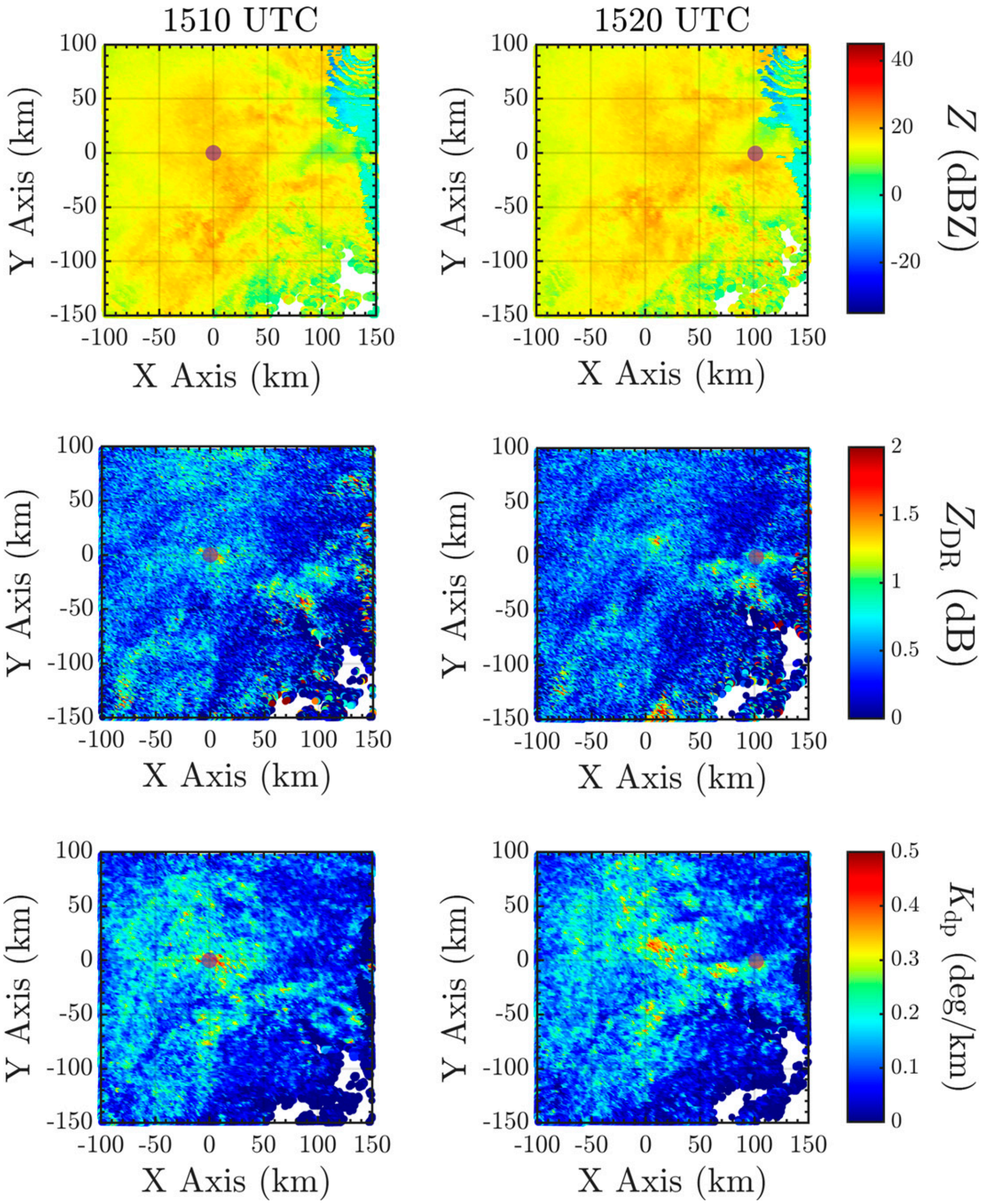

FIG. 2. MRMS horizontal cross sections of (top) Z, (middle) Z_{DR}, and (bottom) K_{dp} at 5 km for (left) 1510 and (right) 1520 UTC during leg 1. Purple dots represent the P3 aircraft locations at each time period. The x and y coordinates are centered on the P3 aircraft location at 1510 UTC. MRMS radar artifacts near the center of a nearby radar can be seen in Z in the top-right corner.

The FCDP and RICE instruments were used to indicate regimes of supercooled liquid drops and the CPI was used along with 3V-CPIview software (SPEC, Inc.) to estimate habit fractions for each leg. While the liquid water content (LWC) estimated from the FCDP was artificially high (up to 200%) due to shattering effects, we use the spikes in FCDP LWC as a way to infer the presence of supercooled liquid droplets. The University of Illinois/Oklahoma OAP Processing Software (UIOOPS; McFarquhar et al. 2018) was used to derive PSDs from the 2DS-V and HVPS-A probes. All 1-Hz PSD samples from the 2DS were ignored when dead time exceeded 70% (i.e., when the 2DS sampled less than 30% of the 1-Hz period). Stricter dead time thresholds would limit the number of time periods with higher concentrations. The remaining samples from the 2DS and HVPS were then averaged in 5-s time intervals for particle sizes in the range 0.1–30 mm where sizes smaller than

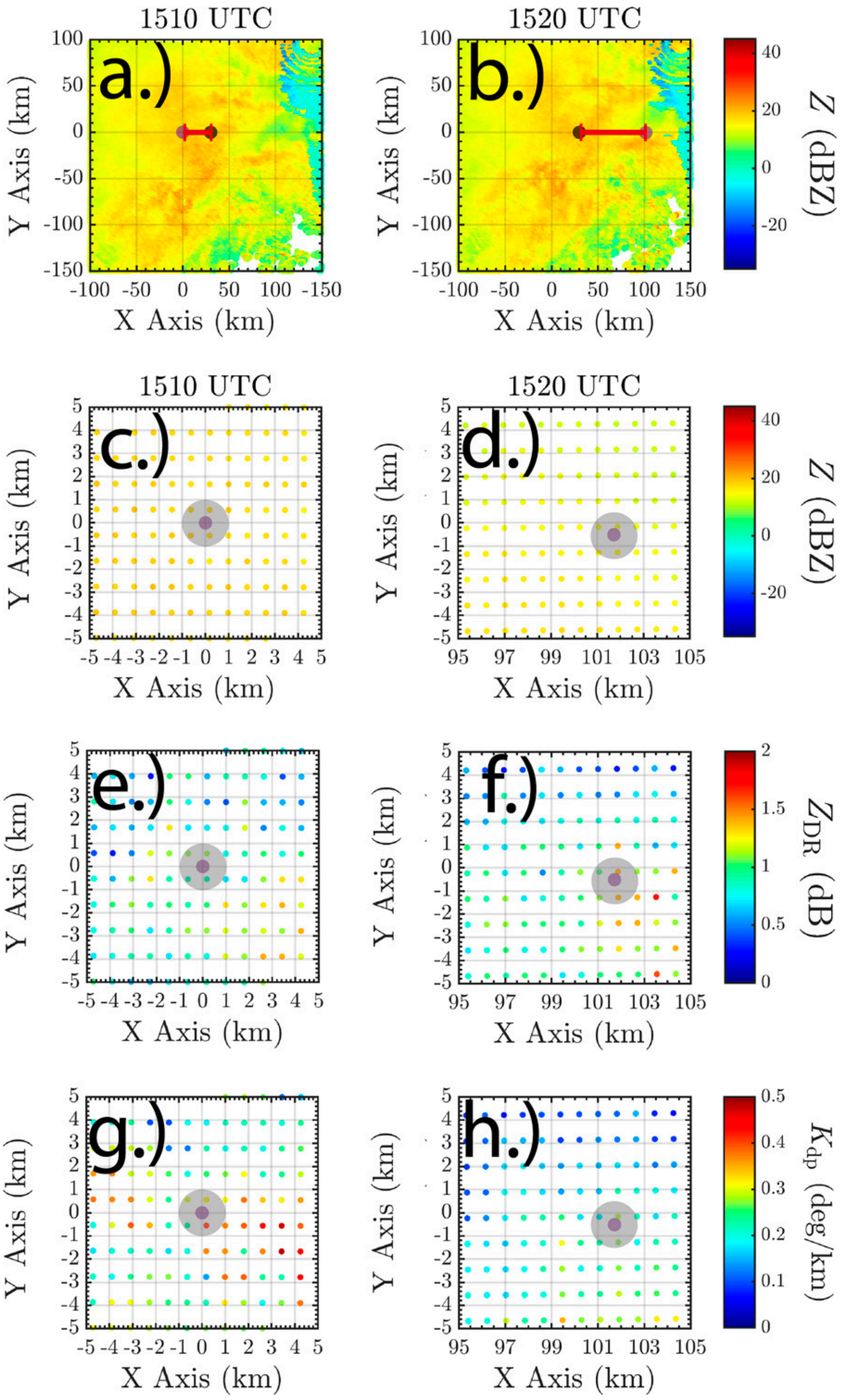

FIG. 3. MRMS horizontal Cartesian cross sections at 5.0 km MSL with P3 locations at MRMS time stamps (a) 1510 and (b) 1520 UTC (purple dots) and a time period in between MRMS time stamps (1513 UTC; black dots). Red lines indicate the temporal contribution to the weighting function, where shorter distances indicate a higher probability for the MRMS time period to be sampled. Also shown are 5.0 km MSL MRMS cross sections (zoomed in) at (left) 1510 UTC and (right) 1520 UTC for (c),(d) reflectivity; (e),(f) Z_{DR}; and (g),(h) K_{dp}. MRMS points within the gray circles represent those of the nearest 1.0 km that are selected during the bootstrap sampling.

1.4 mm used 2DS data, and sizes larger than 1.4 mm used HVPS data. Particle sizes were defined using the circle of minimum enclosure approach $D_{\max}$ of Wu and McFarquhar (2016).

Gamma and exponential distribution fits were performed on the P3 in situ observations for each 5-s binned PSD using the form $n(D_{\max}) = N_{0_s} D_{\max}^{\mu} \exp(-\Lambda_s D_{\max})$. For exponential distributions (i.e., $\mu = 0$), this form is then transformed into its semilogarithmic form: $\ln[n(D_{\max})] = \ln(N_{0_s}) - \Lambda_s D_{\max}$, such that $\ln(N_{0_s})$ and Λ_s was solved by least squares fitting of a first-order polynomial equation. The incomplete gamma moment fitting method of McFarquhar et al. (2015) was used to estimate gamma distribution parameters. In this method, three moments of the in situ observed PSD were numerically calculated that serve as three constraints for estimating μ, N_{0_s}, and Λ_s. Here, we used the zeroth, second, and fourth incomplete moments of the ice-phase PSD because these moments are roughly proportional to ice number, mass, and reflectivity (Ryzhkov et al. 1998) although other moments could be used as well. Even with these moments as PSD parameter constraints, measurement uncertainties and the use of other moments can alter these parameters (McFarquhar et al. 2015). PSD parameters themselves are highly correlated with one another (McFarquhar et al. 2015) and thus any errors in one parameter would manifest in other parameters. Therefore, these parameter estimations are not necessarily unique (i.e., problem of moments) such that even perfect moments can yield multiple plausible parameter sets. In addition, these in situ fits are specifically valid for maximum dimensions between 0.1 and 30 mm, where there is higher confidence in the calculated number concentrations. One set of gamma distribution fits was performed using the aforementioned zeroth, second, and fourth incomplete moments and were compared with the radar retrievals. Large differences between in situ and retrieved N_t can occur because N_t is dominated by concentrations of smaller particles that are not included with the in situ data. Therefore, each radar retrieval used N_t and D_m and a new N_t was diagnosed from integrating the number distribution function from $D_{\max} = 0.1$ mm to $D_{\max} = 30$ mm.

We estimated ice particle aspect ratios by fitting ellipses to each particle image. Ellipse fits and corresponding ellipse orientation angles were computed using the Computational Geometry Algorithms Library (CGAL) C++ library functions and the methodology of Welzl (1991) and Gärtner and Schönherr (1998) to find the ellipse of the smallest area enclosing a finite set of points. Ellipse orientation angles are defined as the angle between the maximum dimension and the time dimension (i.e., flight direction). Aspect ratio statistics were only computed for particle images that were fully within the probe sampling volume. Ellipse fits were computed from the horizontally and vertically oriented HVPS and 2DS datasets. While radar retrieval calculations used the actual intrinsic (spheroid) aspect ratios, these in situ ellipse fits represent 2D projections of each ice particle. Therefore, the projected ellipse fit aspect ratio Φ can be in the range $\varphi \leq \Phi \leq 1.0$ depending upon particle orientations as imaged by the in situ cloud probes.

IWC was estimated from the observed PSDs following two different methods. The first method adopted a modified form of the static m–D relationship from Brown and Francis (1995, hereinafter BF95) as described in Hogan et al. (2012). The second method employed scattering simulations of varying riming degrees and m–D relations from Leinonen and Szyrmer (2015, hereinafter LS15) to determine the m–D relation that best minimized the reflectivity difference between ER2 HIWRAP radar measurements at the P3 location and that simulated from the PSDs for each 5-s interval. Unless otherwise noted, the majority of results use the BF95 IWC calculations since LS15 calculations are only available when the ER2 and P3 were less than 4 km apart horizontally and when data were within 3 min of each other.

c. *Radar retrieval methodology*

Radar retrieval equations used in this work come primarily from two sources: Ryzhkov and Zrnić (2019, hereinafter RZ19) and Bukovčić et al. (2020, hereinafter B20), with the exception of the nonpolarimetric IWC retrieval from Hogan et al. (2006, hereinafter H06) that uses Z (dBZ) and temperature in degrees Celsius. RZ19 and B20 assume that particles are described in terms of equivolume diameters D and are represented as oblate spheroids with fixed aspect ratios: $\varphi = b/a \approx \overline{\varphi}$ where b and a are the spheroid semiminor and semimajor axis lengths, respectively. Korolev and Isaac (2003) found that stratiform (predominantly irregular and aggregate) precipitation particle projected aspect ratios depend slightly on particle size where most projected aspect ratios fall in the range $0.6 \leq \Phi \leq 0.8$. Many laboratory and in situ aircraft studies have, however, demonstrated power-law behavior of pristine habit shape with size (Auer and Veal 1970; Lamb and Scott 1972; Um et al. 2015). As a result, we would expect that RZ19 and B20 retrievals would be most consistent with observations for cloud systems dominated by irregular or aggregate particles rather than pristine particles such as dendrites or columns. From RZ19 and B20, there are two separate methodologies for retrieving D_m, N_t, and IWC from the radar variables. RZ19 describe an approach using Z, Z_{DR}, and K_{dp} (three variables), whereas B20 uses Z and K_{dp} (two variables). While RZ19 also describe the B20 approach, we refer to RZ19 as the three-variable approach, whereas we refer to B20 as the two-variable approach for simplicity. Each equation we use is derived in the same way as RZ19 and B20 with the exception that we relax the PSD form to be that of a gamma distribution rather than an exponential distribution. Derivations for these equations are given in appendix. Table 1 provides the general retrieval equations as well as the simplified forms provided by RZ19 and B20. These simplified forms assume fixed values of $\overline{\varphi}$, the density–size power-law prefactor α, and the axisymmetric Gaussian orientation standard deviation σ and assume $\mu = 0$. Notice that the RZ19 retrievals use a quantity called Z_{dp}, which is the *linear* difference in horizontal and vertical reflectivity: $Z_{\mathrm{dp}} = Z_h - Z_v$ rather than strictly Z_{DR}. This is because, to first order, Z_{dp} is conveniently proportional to the third moment of the size distribution (see the appendix). This means that Z_{dp} is related to Z_{dr} and Z_h as $Z_{\mathrm{dp}} = Z_h(1 - Z_{\mathrm{dr}}^{-1})$.

Notice that each of the general equations presented in Table 1 are expressed in terms of a multivariate power-law relation: $F = cK_{\mathrm{dp}}^{d_{k_{\mathrm{dp}}}} Z_{\mathrm{dp}}^{d_{z_{\mathrm{dp}}}} Z_h^{d_{z_h}}$, where F is D_{m}, N_t, or IWC.

TABLE 1. Table of retrieval equations used in this paper: D_m is in units of millimeters, N_t is in units of number per meter cubed, and IWC is in units of grams per meter cubed; F_s is the combined shape/orientation factor that depends upon $\overline{\varphi}$ and σ. See the appendix for more details.

Methodological source	Variable	Equation
RZ19	D_m	$\frac{0.54}{\lambda^{1/2}}\alpha^{-1/2}\frac{\mu+4}{\sqrt{(\mu+3)(\mu+2)}}K_{\mathrm{dp}}^{-1/2}Z_{\mathrm{dp}}^{1/2}$
	N_t	$53.8\lambda^2\frac{(\mu+3)(\mu+2)}{(\mu+4)(\mu+1)}K_{\mathrm{dp}}^2Z_{\mathrm{dp}}^{-2}Z_h$
	IWC	$8.0\times10^{-3}\lambda\frac{\mu+2}{\mu+4}K_{\mathrm{dp}}Z_{\mathrm{dp}}^{-1}Z_h$
RZ19 (simplified) $\mu = 0$ and $\alpha = 0.2$ g cm^{-3} mm	D_m (fit)	$-0.1+2.0\sqrt{Z_{\mathrm{dp}}/(\lambda K_{\mathrm{dp}})}$
	N_t	$80.7\lambda^2K_{\mathrm{dp}}^2Z_{\mathrm{dp}}^{-2}Z_h$
	IWC	$4.0\times10^{-3}\lambda K_{\mathrm{dp}}Z_{\mathrm{dp}}^{-1}Z_h$
B20	D_m	$0.924\left[\frac{(\mu+4)^2}{(\mu+3)(\mu+2)}\right]^{1/3}\left(\frac{F_s}{\lambda}\right)^{1/3}K_{\mathrm{dp}}^{-1/3}Z_h^{1/3}$
	N_t	$\frac{6.14}{\alpha^2}\frac{[(\mu+4)(\mu+3)(\mu+2)]^{1/3}}{\mu+1}\left(\frac{\lambda}{F_s}\right)^{4/3}K_{\mathrm{dp}}^{4/3}Z_h^{-1/3}$
	IWC	$\frac{0.0027}{\alpha}\left[\frac{(\mu+2)^2}{(\mu+4)(\mu+3)}\right]^{1/3}\left(\frac{\lambda}{F_s}\right)^{2/3}K_{\mathrm{dp}}^{2/3}Z_h^{1/3}$
B20 (simplified) $\mu = 0$, $\alpha = 0.178$ g cm^{-3} mm, $\lambda = 110.8$ mm (S band), $\overline{\varphi} = 0.65$, and $\sigma = 0°$	D_m	$0.15K_{\mathrm{dp}}^{-1/3}Z_h^{1/3}$
	N_t	$2.93\times10^6K_{\mathrm{dp}}^{4/3}Z_h^{-1/3}$
	IWC	$0.77K_{\mathrm{dp}}^{2/3}Z_h^{1/3}$
H06	IWC	$10^{0.060Z(\mathrm{dBZ})-0.0212T(^\circ\mathrm{C})-1.92}$

Because these relations are analytic, it is natural to explore how uncertainties in each radar quantity affect each retrieval. These uncertainties are important in order to properly evaluate the performance of each retrieval equation and to optimize the microphysical parameters (i.e., F_s, μ, and α) in Table 1. To first order and ignoring correlations between each radar variable, retrieval uncertainties can be expressed through differentiating each retrieval equation with respect to each radar variable using the variance "propagation of uncertainty" equation

$$\begin{aligned}\frac{\sigma_F}{F} &= \frac{1}{F}\sqrt{\left(\frac{\partial F}{\partial K_{\mathrm{dp}}}\right)^2\sigma_{K_{\mathrm{dp}}}^2+\left(\frac{\partial F}{\partial Z_{\mathrm{DR}}}\right)^2\sigma_{Z_{\mathrm{DR}}}^2+\left(\frac{\partial F}{\partial Z}\right)^2\sigma_Z^2}\\ &= \sqrt{d_{k_{\mathrm{dp}}}^2\left(\frac{\sigma_{K_{\mathrm{dp}}}}{K_{\mathrm{dp}}}\right)^2+d_{z_{\mathrm{dp}}}^2\frac{(\ln 10)^2}{100}\left(\frac{Z_{\mathrm{DR}}}{10^{Z_{\mathrm{DR}}/10}-1}\right)^2\left(\frac{\sigma_{Z_{\mathrm{DR}}}}{Z_{\mathrm{DR}}}\right)^2+(d_{z_{\mathrm{dp}}}+d_{z_h})^2\frac{(\ln 10)^2}{100}\sigma_Z^2},\end{aligned} \tag{3}$$

where σ_X represents the standard deviation of MRMS quantities and retrievals. Notice that B20 relations have relative errors that only depend upon the relative error in K_{dp} and the absolute error (in dB) of Z (i.e., $d_{z_{\mathrm{dp}}} = 0$), whereas the

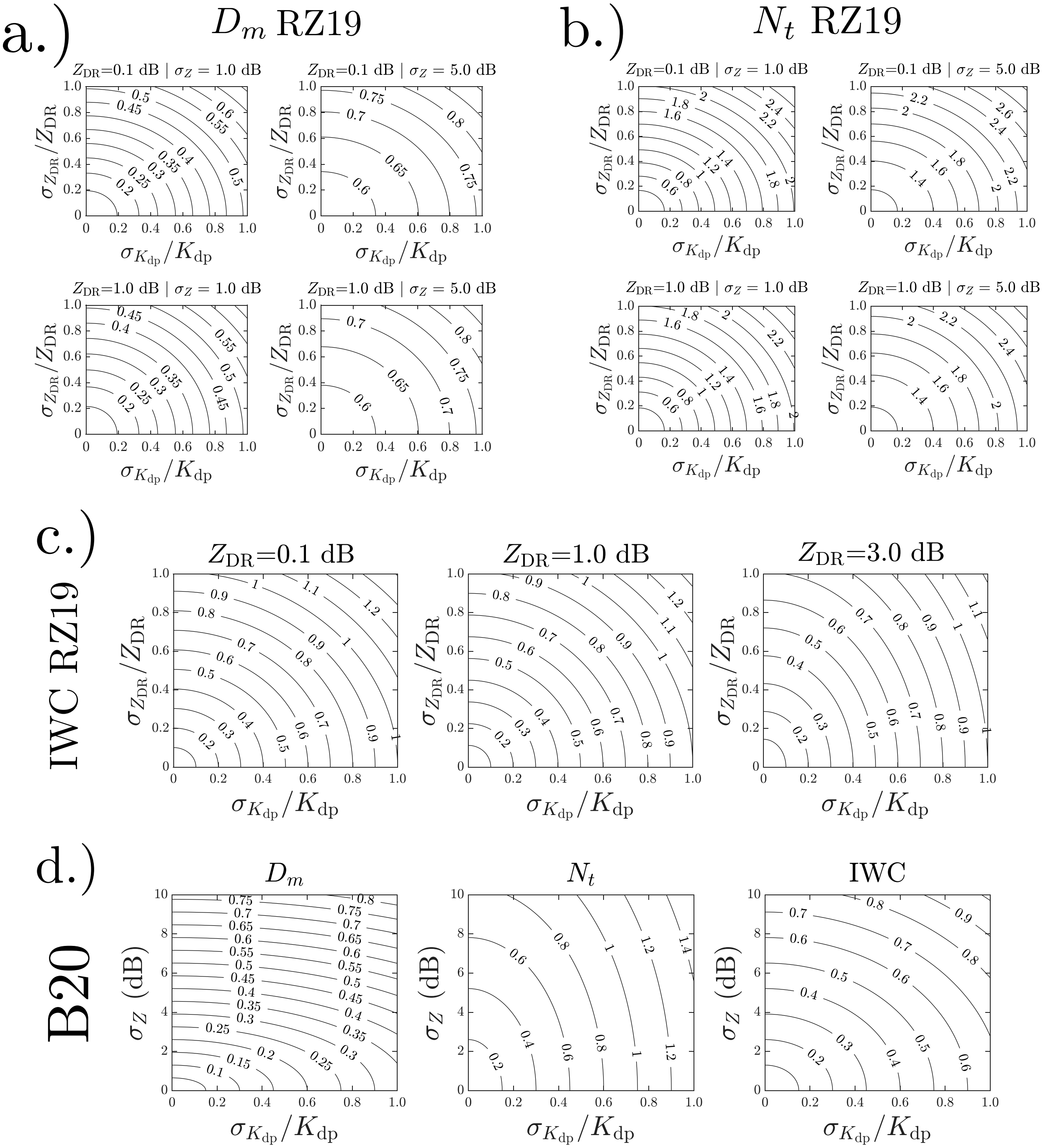

FIG. 4. Relative error contours for D_m (increments of 0.05), N_t (increments of 0.2), and IWC (increments of 0.1) retrievals using Eq. (3) and Table 1 for different values of $\sigma_{K_{\rm dp}}/K_{\rm dp}$, $\sigma_{Z_{\rm DR}}/Z_{\rm DR}$, and σ_Z: (a) relative errors of D_m in terms of σ_{D_m}/D_m using RZ19 retrievals for different values of $Z_{\rm DR}$ and σ_Z, (b) as in (a), but for N_t, (c) relative errors of IWC using RZ19 for different values of $Z_{\rm DR}$, and (d) relative errors in D_m, N_t, and IWC using B20.

RZ19 relation errors depend upon relative errors in $K_{\rm dp}$ and $Z_{\rm DR}$ as well as the the absolute error of Z and $Z_{\rm DR}$. While there are certainly correlations between (for instance) Z and $K_{\rm dp}$, we use Eq. (3) as a simple way to estimate the propagation of error for assumed radar variable errors resulting from calibration biases and spatiotemporal uncertainties.

Figure 4 shows contours of D_m, N_t, and IWC relative uncertainties for various ranges of each independent variable in Eq. (3).

Figure 4a shows that RZ19 retrievals of D_m depend equally on relative uncertainties in both Z_{DR} and K_{dp} with relative errors strongly dependent upon the absolute Z uncertainty and weakly dependent on the magnitude of Z_{DR}. Overall D_m uncertainties for $\sigma_Z \le 5.0$ dB are less than unity as long as relative uncertainties of Z_{DR} and K_{dp} are also less than unity. The N_t uncertainties (Fig. 4b) mirror the contours of D_m uncertainties but are 2–4 times as large. RZ19 IWC retrievals (Fig. 4c) also depend equally on Z_{DR} and K_{dp} relative errors but do not depend upon Z uncertainties. If Z_{DR} is small (i.e., 0.1 dB), the relative errors of IWC depend equally upon the relative errors in Z_{DR} and K_{dp}. Greater values of Z_{DR} stretch IWC errors along the $\sigma_{Z_{\mathrm{DR}}}/Z_{\mathrm{DR}}$ axis in Fig. 4c. For small relative errors in K_{dp}, increasing Z_{DR} from 0.1 to 3.0 dB increases relative errors in IWC by almost 0.2. Figure 4d shows that B20 retrieval errors of D_m depend heavily on absolute errors in Z as compared with relative errors in K_{dp}, whereas B20 N_t relative errors depend more on relative errors in K_{dp} than σ_Z. B20 IWC relative errors depend heavily upon both K_{dp} relative errors and Z absolute errors. Overall, B20 errors are generally lowest with D_m and highest with N_t.

To compare the observed size distributions with the radar retrievals, it is necessary to ensure consistency in the definition of the chosen particle size (McFarquhar and Black 2004; Wu and McFarquhar 2016). The radar retrievals use equivolume diameter D, whereas the in situ observations are in terms of the maximum dimension $D_{\max}$, which is the minimum diameter of an enclosing circle based on the particle projections measured by the 2DS and HVPS instruments. Here, we perform radar retrievals of D_m and then use size distribution continuity [i.e., $n(D)dD = n(D_{\max})dD_{\max}$] to retrieve mean volume diameters in terms of maximum dimension

$$D_{m,\max} = D_m \overline{\varphi}^{-1/3}. \tag{4}$$

Although the apparent maximum dimensions and aspect ratios from in situ observations depend upon particle orientations (McFarquhar et al. 1999; Jiang et al. 2017; Dunnavan and Jiang 2019) that can be influenced by the cloud probe itself (King 1985, 1986), the use of maximum dimension here acts as a simple way to compare radar retrievals with in situ observations. It is important to note that, neglecting any optical errors, truly spheroidal particles will have either their semimajor (oblate) or semiminor (prolate) axis lengths represented in their 2D ellipse projections due to axis symmetry. Therefore, we would expect that only prolate-like, or triaxial particles would exhibit errors in $D_{\max}$, whereas oblate-like or planar crystals would have apparent maximum dimensions that differ strictly only to morphological effects (e.g., asymmetric branch structure).

Aspect ratio retrievals are performed following the methodology of Matrosov et al. (2020) where a proxy for circular depolarization ratio (CDR_p) is used to estimate $\overline{\varphi}$. CDR_p is constructed from Z_{dr} and ρ_{hv} such that

$$\mathrm{CDR}_p = 10 \log\left(\frac{Z_{\mathrm{dr}} + 1 - 2\sqrt{Z_{\mathrm{dr}}}\rho_{\mathrm{hv}}}{Z_{\mathrm{dr}} + 1 + 2\sqrt{Z_{\mathrm{dr}}}\rho_{\mathrm{hv}}}\right). \tag{5}$$

To estimate $\overline{\varphi}$, pairs of D_m and $\overline{\varphi}$ are used in Eqs. (A7a), (A7b), and (A7e) to explicitly calculate CDR_p with Eq. (5). A gridded interpolant function is then fit to the calculated $\mathrm{CDR}_p(D_m, \overline{\varphi})$ surface from which radar-retrieved simplified RZ19 D_m values (Table 1) and estimated values of CDR_p are then inverted to estimate $\overline{\varphi}$. For both RZ19 and B20 retrieval methodologies, aspect ratio retrievals are inverted using the RZ19 retrieval because D_m does not depend upon $\overline{\varphi}$. Aspect ratio retrievals using this methodology are expected to have errors that could be at least 0.2 (Matrosov 2020).

Notice from Table 1 that the general retrieval equations for B20 depend directly upon μ, α and F_s (which itself depends on $\overline{\varphi}$ and σ), whereas RZ19 does not depend at all on F_s and only depends upon α when retrieving D_m. Furthermore, RZ19 $D_{m,\max}$ only implicitly depends on $\overline{\varphi}$ due to the Eq. (4) conversion and N_t from integrating from $D_{m,\max} = 0.1$ mm to $D_{m,\max} = 30$ mm. Therefore, while the RZ19 retrieval methodology conveniently does not substantially depend upon these extra parameters, it is more difficult to reconcile any discrepancies between in situ measurements and MRMS retrievals. B20 retrievals, on the other hand, have at least four parameters that could help explain any possible retrieval discrepancy among the three retrieved quantities. As a result, we provide an additional set of B20 retrievals using a cascaded, ensemble Markov chain Monte Carlo (MCMC) MATLAB program (Grinsted 2022) based on the Goodman and Weare (2010) affine invariant MCMC algorithm. This MCMC program is used to explore the parameter space of B20 variables, thus allowing us to infer the best parameter sets to use and how parameters are correlated with one another. The MCMC code works by specifying a log-likelihood function (i.e., a cost function) for a given set of observations (in this case, D_m, N_t, and IWC) and a model (in this case, the B20 retrievals). The log-likelihood function incorporates both the mean quantities as well as errors from both the in situ measurements and the MRMS bootstrapping. In situ measurement errors are estimated following Finlon et al. (2019) who uses Poisson statistics to estimate the standard deviation of the number distribution function for each size bin. MRMS errors are incorporated by converting bootstrap covariance matrices of Z and K_{dp} to standard deviations of $D_{m,\max}$, N_t, IWC through a variant of Eq. (3) for Z_h and K_{dp}. Then, 50 random walkers are generated with initial values of α, $\overline{\varphi}$, σ, and μ. The MCMC program calculates the log-likelihood function for each walker as each walker samples various retrieval parameters with acceptance probability dependent upon the log-likelihood ratio of proposal to current sample. Each random walker chains together 130 000 parameter samples each for every 5-s time period of leg 1 and leg 2. The resulting posterior distribution of parameters then represents the four-dimensional (α, $\overline{\varphi}$, σ, and μ) or three-dimensional (α, $\overline{\varphi}$, and σ) probability space of all parameters. For more details, see Goodman and Weare (2010).

5. Results

a. In situ measurements and MRMS collocation

Time–height profiles of Z, Z_{DR}, K_{dp}, and CDR_p are shown in Fig. 5 for legs 1 and 2 using the bootstrapping procedure

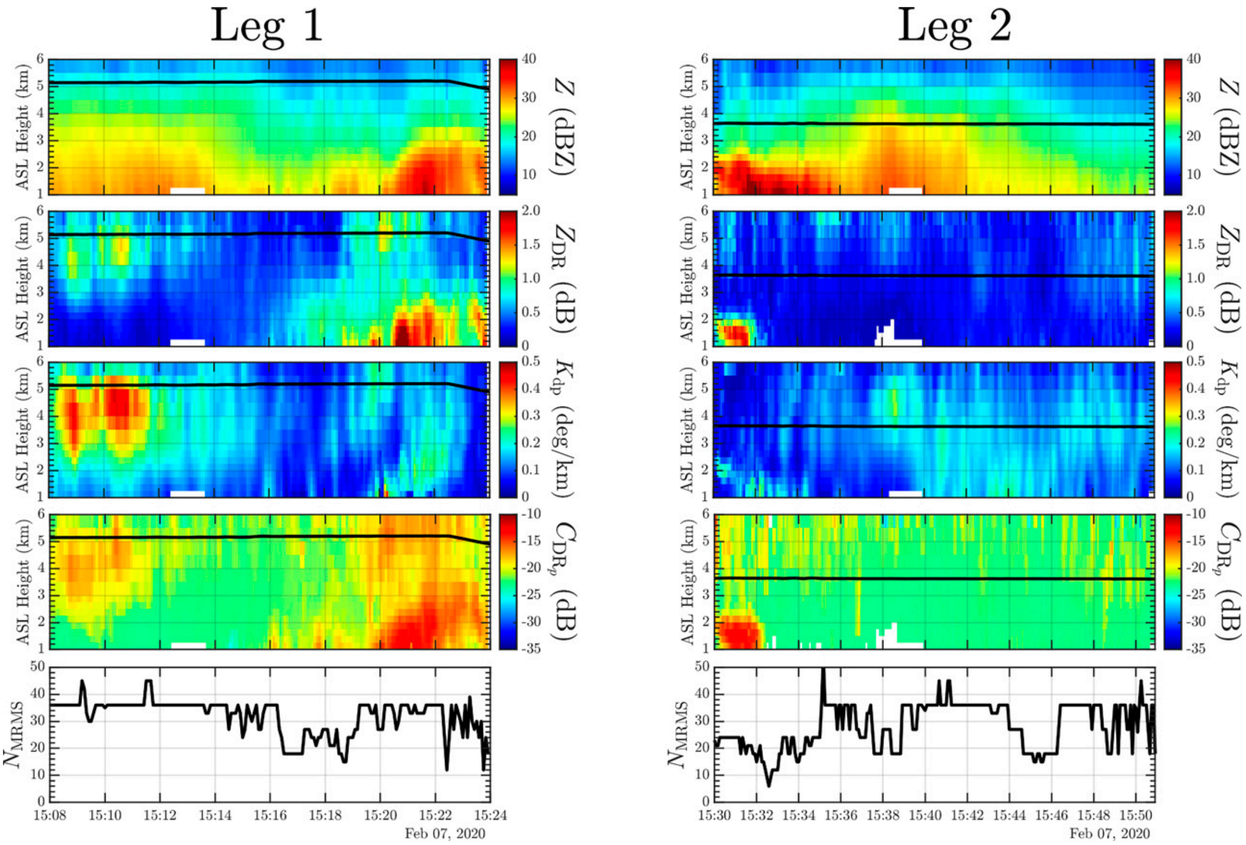

FIG. 5. (top four rows) MRMS data collocated along the P3 aircraft flight path latitude and longitude (thick, black line) for (left) leg 1 and (right) leg 2. Also shown are (bottom) the number of unique MRMS grid points used for collocation with P3 aircraft.

described in section 4c. Figure 5 shows a classic dendritic growth layer enhancement region in Z_{DR}, K_{dp}, and CDR_p from 1508 to 1512 UTC (with a maximum at approximately 1510:30 UTC). Values of K_{dp} in particular are quite high and approach values of 0.5° km^{-1} along the P3 flight path. A weaker K_{dp}, but higher Z_{DR} enhancement region can be seen later from approximately 1520 UTC, which lies just above the frontal boundary on the easternmost portion of leg 1 (Fig. 1). During leg 2, the P3 aircraft flew at a lower altitude (higher temperature). As such, enhanced aggregation at this lower level contributed to larger Z and diminished K_{dp} and Z_{DR} relative to leg 1.

A *GOES-16* multichannel imaging algorithm (MIA; Hu et al. 2021) and CPI particle images suggests that the first K_{dp} and Z_{DR} peak at 1510 UTC was primarily dominated by irregular dry ice particles, whereas the second peak at 1520 UTC corresponds to a large number of small, supercooled liquid droplets mixed together with ice particles. In Fig. 6, "irregular" particles (i.e., polycrystalline) constitute approximately 60% of all particles throughout each leg except during regions close to the frontal boundary where "spheroidal" particles, indicative of supercooled liquid droplets, occasionally dominate the observed particle type in conjunction with peaks in FCDP LWC measurements. While the 3V-CPIview software used to perform these habit classifications is not perfect because of misclassification of planar crystals and dendrites (such particles would normally be classified in the "plates" category but were instead misclassified as "rosettes"), casual observation of CPI images indicate that irregular polycrystals and spatial planar crystals do dominate the majority of ice throughout both legs. In addition, the RICE frequency behavior during this leg shows sharp frequency decreases (indicating the presence of liquid particles) at various times. Despite the P3 flying below cloud top, both MIA and RICE observations (Fig. 6) show a sharp transition from a dry ice environment to a mixed-phase environment around 1520 UTC. The correspondence between MIA and P3 observations appears to even capture the sharp spikes of LWC that are estimated from the FCDP data at 1521 UTC in Fig. 6. In particular, FCDP size distributions for 1521 UTC illustrate a pronounced peak at 25 μm, which is indicative of liquid droplets (Cober et al. 2001; McFarquhar et al. 2007). The appearance of this peak corresponds to a FCDP number concentration of 19 cm^{-3} (not shown). At 1510 UTC, on the other hand, the FCDP measured number concentration values that were fewer by a factor of approximately 6 (3 cm^{-3}) and there was no pronounced peak. Therefore, the K_{dp} and Z_{DR} peaks shown at 1510 UTC and 1520 UTC in Fig. 5 suggest two different microphysical regimes where 1510 UTC represents a population of dry ice, and 1520 UTC represents a population of supercooled liquid droplets and ice particles.

Figure 7 shows the time series of bulk parameters $D_{m,\max}$ and N_t from the P3 observations and the exponential and

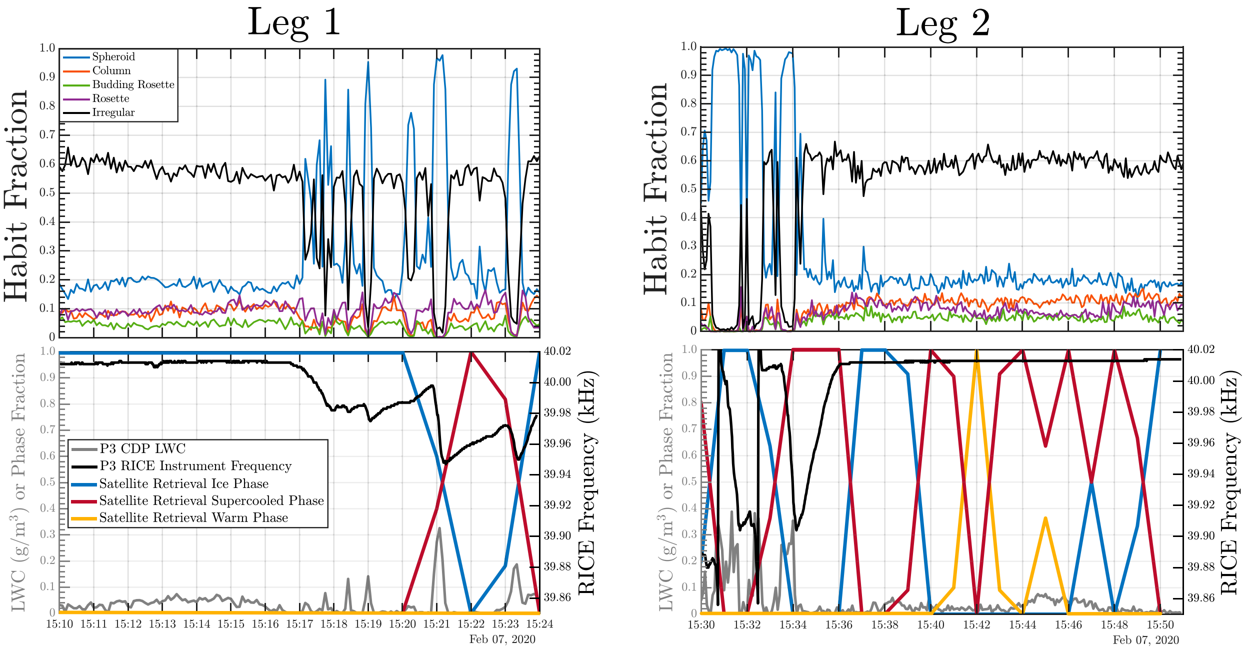

FIG. 6. (top) CPI-derived habit fractions for (left) leg 1 and (right) leg 2. Plates were not identified for either leg and thus were not included in the plot. (bottom) Time series phase fractions of ice (blue), supercooled liquid droplets (red), and liquid water (yellow) as estimated by MIA for (left) leg 1 and (right) leg 2. Also shown are P3 estimates of LWC (gray) from the FCDP instrument and the RICE (black) frequency.

gamma PSD fits. These plots not only show the *observed* values of $D_{m,\max}$ and N_t that will be used to evaluate MRMS retrieval performance, but they also show how well the exponential PSD and gamma PSD forms can capture the measured PSDs. Exponential PSD fits ($\mu = 0$) tend to overestimate $D_{m,\max}$ by at least 0.3 mm and underestimate N_t by as much as 20 L^{-1}. Therefore, errors in the exponential fitting alone can account for at least 50% of the observed N_t values. Using a gamma distribution (with variable μ) dramatically improves the PSD fit where N_t can be captured to within a few numbers per liter for a majority of each flight leg and $D_{m,\max}$ can be captured well within 0.1 mm. The μ is generally positive for a majority of leg 1 and for the last part of leg 2. Negative μ values are apparent during periods of supercooled liquid droplets in leg 1 (e.g., 1521 UTC) and leg 2 before 1538 UTC.

The Z_{DR} and K_{dp} during leg 1 are positively correlated with N_t for the dry ice period (Fig. 8) where the K_{dp} and Z_{DR} peak at 1510 UTC corresponds to a N_t peak, whereas the later K_{dp} and Z_{DR} peak at 1520 UTC does not show this correlation. From 1508 to 1518 UTC, correlation coefficients between N_t and the MRMS radar variables are 0.77 and 0.81 for K_{dp} and Z_{DR}, respectively. While leg-1 reflectivities are generally higher during the first peak at 1510 UTC than during the second peak at 1520 UTC, the correlation between N_t and Z (0.48) is not as strong as with K_{dp} or Z_{DR} from 1508 to 1518 UTC. The correlation coefficients for the entirety of leg 1 are overall lower for K_{dp}, Z_{DR}, and Z (0.48, 0.16, and 0.45, respectively), whereas leg-2 correlations from 1530 to 1551 UTC are lower as well (0.43, 0.24, and −0.11, respectively). Size distributions for the 1510 UTC period (not shown) illustrate that the maximum dimensions of the particles corresponding to the N_t peak are between 0.1 and 1.0 mm, with a mean maximum dimension of approximately 0.5 mm.

Ellipse fit joint distributions of major dimension and aspect ratio (Fig. 9) suggest that particles are apparently very spherical at all sizes for both the 1510 UTC period and the entirety of leg 1. While dendrites or other anisotropic particles could yield high ellipse fit aspect ratios if they are preferentially viewed along their faces, the observed small sizes instead suggest that the numerous particles responsible for the first K_{dp} and Z_{DR} enhancement region between 1510 and 1512 UTC are either hexagonal plates or irregular particles consistent with the hypothesis of Moisseev et al. (2015), Griffin et al. (2018) and others or secondary ice production (e.g., Andrić et al. 2013). CPI images and the CPI classification algorithm shown in Fig. 6 suggests that there is no substantial change in habit type throughout the first K_{dp} and Z_{DR} enhancement region. This is somewhat surprising considering that these enhancement regions could result strictly from changes in particle properties alone. Unlike in Griffin et al. (2018), the Z_{DR} and K_{dp} during leg 1 are generally correlated, which suggests perhaps that both signatures were the result of the same or similar particle types. However, ρ_{hv} (not shown) indicates a brief, sharp decrease from 1510:10 to 1510:40 UTC and reaches a low value of almost 0.96. Thus, it is possible that some or all of the 1510 UTC K_{dp} and Z_{DR} peak results from particles that are, for instance, denser than the observed irregular particles from Fig. 6. For example, this decrease in ρ_{hv} could result from secondary ice production such as from the collisional breakup of ice particles. The second K_{dp} and Z_{DR} peak occurred at lower N_t and Z values (Fig. 8), which suggests that lower cloud tops with less numerous but larger anisotropic particles like dendrites were not masked as much by the presence of larger, more spherical

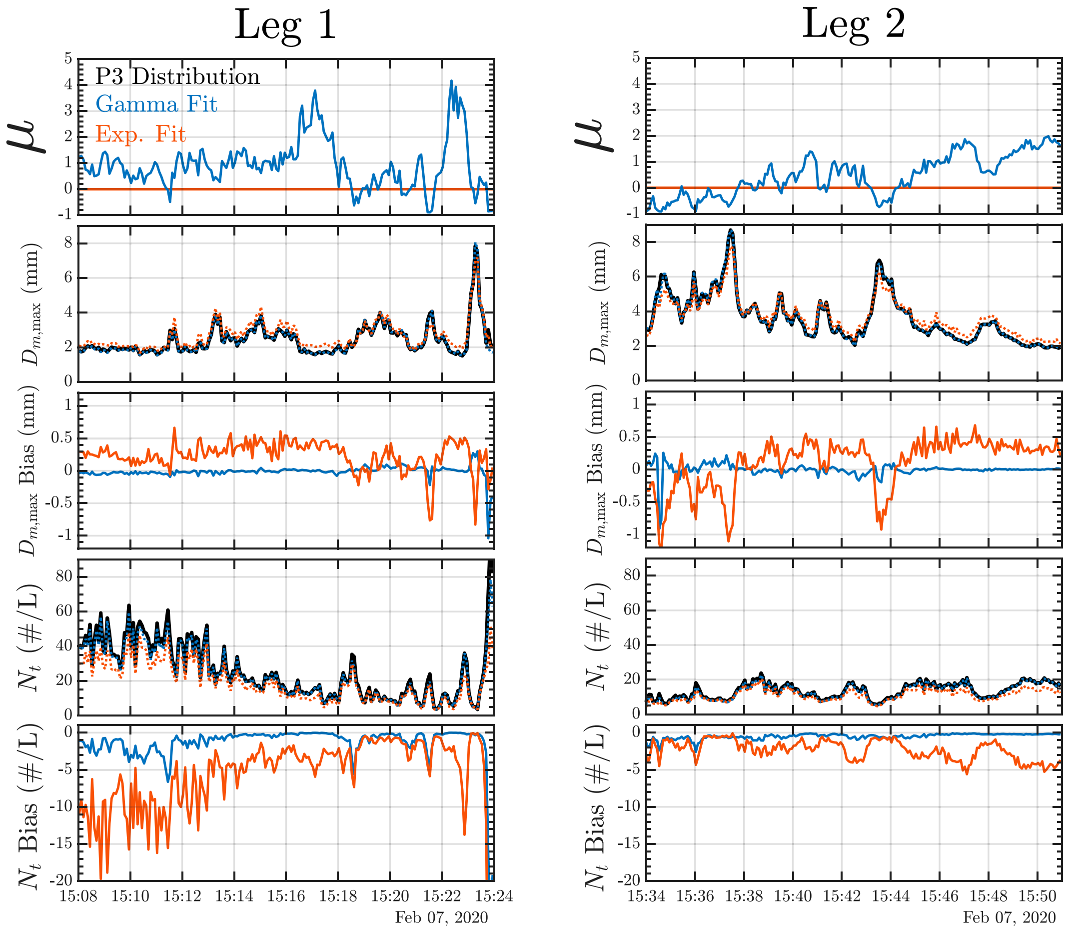

FIG. 7. PSD measurements of $D_{m,\max}$ and N_t computed directly from measured PSDs from the 2DS and HVPS (black lines), gamma distribution fits (blue lines), and exponential distribution fits to the 2DS/HVPS PSDs (orange lines) for (top) μ, (top middle) $D_{m,\max}$, (middle) $D_{m,\max}$ bias, (bottom middle) N_t, and (bottom) N_t bias for (left) leg 1 and (right) leg 2; $D_{m,\max}$ and N_t biases represent P3 probe observations subtracted from fits to the P3 probe observations. Fit parameters $D_{m,\max}$ and N_t were calculated over the 2DS and HVPS size range ($0.10 \leq D_{\max} \leq 30.0$ mm) representing the P3-observed PSD.

particles (Griffin et al. 2018). This leads to Z_{DR} being larger at 1520 UTC than during the 1510 UTC peak but with lower K_{dp} due to lower N_t at 1520 UTC. Particle images indicate local peaks in $D_{m,\max}$ shown in Fig. 7 are the result of large aggregates, irregular particles, and/or dendrites.

b. MRMS radar retrieval results

Figure 10 shows the leg-1 and leg-2 distributions of relative error for $D_{m,\max}$, N_t, and IWC. Simplified retrievals (Fig. 10a) consistently underestimate $D_{m,\max}$ by approximately 50% for both legs. The N_t is consistently overestimated where RZ19 errors are less than B20. Both N_t and IWC relative error distributions are heavily skewed to larger, more positive relative errors, especially for leg 2 where retrievals are heavily biased during the 1530–1534 UTC period of supercooled liquid droplets (Fig. 6) where in situ measured IWC values are very low. The median relative errors of RZ19 N_t and IWC for leg 1 are small (+17% and −2%, respectively) but are much larger, and more positive, for leg 2 (+110% and +75%, respectively). B20 median relative errors are consistently larger overall for both N_t (+117%) and IWC (+43%)

Retrieved aspect ratios from the Matrosov (2020) CDR$_p$ retrieval methodology (Fig. 10b) for each leg are very low ($0.1 \leq \overline{\varphi} \leq 0.2$) and, unlike the N_t and IWC retrievals, are approximately Gaussian for both RZ19 and B20 methodologies. These low aspect ratios are surprising considering that ice particles for both legs are predominantly irregular (Fig. 6) with mean ellipse fit aspect ratios that are approximately 0.7 for all sizes (Fig. 9). Despite this inconsistency, general retrievals using these aspect ratios overall substantially decrease the $D_{m,\max}$ magnitude of the median relative errors for the RZ19 methodology (−17%) due to the D_m-to-$D_{m,\max}$ conversion [Eq. (4)]. As shown in Table 1, RZ19 retrievals of D_m, N_t, and IWC do not directly depend upon $\overline{\varphi}$ or σ, and α only affects D_m. Therefore, these improvements affect only $D_{m,\max}$ and have no effect on IWC

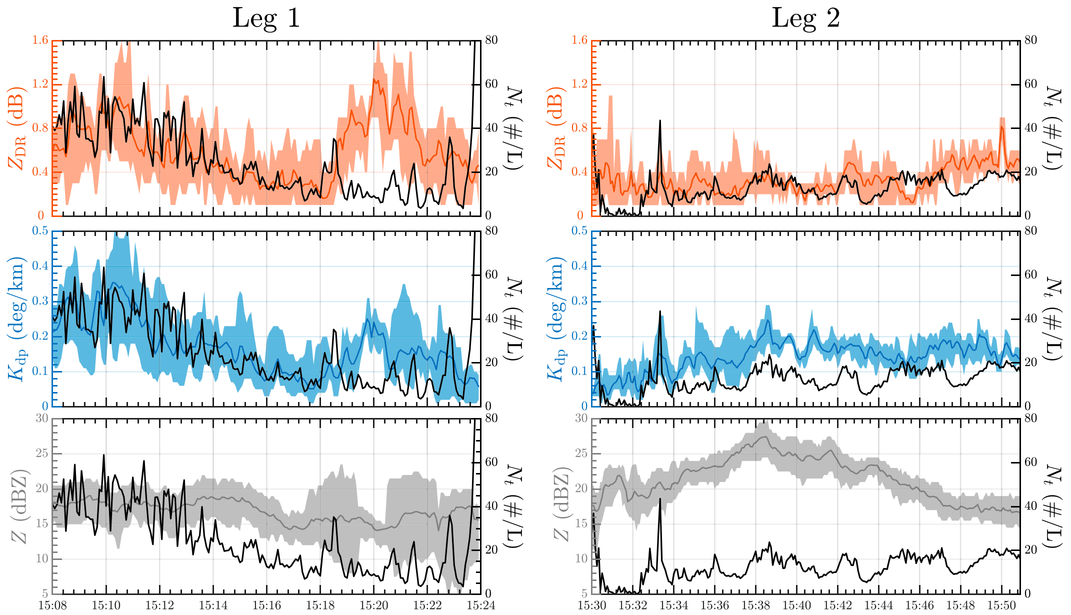

FIG. 8. (left) Leg-1 and (right) leg-2 time series of (top) Z_{DR}, (middle) K_{dp}, and (bottom) Z along with the P3 probe N_t calculations from Fig. 7. Shaded regions represent the 5th–95th-percentile range of MRMS bootstrap samples.

whatsoever. B20 retrievals with these retrieved aspect ratios not only improve the leg-1 and leg-2 magnitude of the median relative errors for $D_{m,\max}$ (+35% and +28%, respectively), N_t (−54% and −47%, respectively), and IWC (−43% and −13%, respectively) but also substantially decrease the overall spread of N_t and IWC relative errors throughout each leg.

Figure 11 compares the IWC MRMS retrievals from the two simplified polarimetric methods shown in Table 1 and the nonpolarimetric method (H06) with the BF95 and LS15 in situ measurements. H06 retrievals using the ER2 EXRAD reflectivity are also included for comparison as well. For leg 1, RZ19 retrievals are by far the most consistent with observations, whereas B20 overestimates IWC by approximately 50% and the H06 retrievals underestimate IWC by approximately 50%. Unlike the nonpolarimetric H06 retrievals, both the RZ19 and B20 simplified retrieval methodologies capture the correct trend where IWC fluctuates at higher values from 1508 to 1515 UTC and then decreases from 1515 to 1518 UTC. B20 is overall biased more to larger IWC values than RZ19 for both legs and in situ IWC estimates and thus produces larger overall errors. The H06 methodologies generally underestimate IWC relative to observations by approximately 50% for the majority of the leg-1 dry ice half but more consistently captures the observed low IWC values during the supercooled liquid droplet period around 1520 UTC. Using the ER2 EXRAD reflectivity does improve the IWC retrievals but only by about 10%. During leg 2, both RZ19 and B20 on average overestimates IWC by well over 50%, whereas both H06 retrievals on average captures IWC to within 50% of both sets of in situ measurements.

B20 RETRIEVALS WITH OPTIMIZED PARAMETERS

While the previous section evaluated the simplified approaches with assumed parameters for α and σ, it is natural to wonder how well retrievals could capture the measured $D_{m,\max}$, N_t, and IWC if each assumed parameter varies. To investigate such optimal parameter sets, we use MCMC runs along with the general B20 equations from Table 1 such that all three parameters: $\overline{\varphi}$, α, and σ are varied from their assumed values. In addition, we also vary μ as an additional parameter along with the common $\mu = 0$ assumption. Figure 12 shows leg-1 and leg-2 time series of the MCMC-optimized parameters that are drawn from the collated joint posterior probability distribution from each leg. These joint probability distributions are combined from each 5-s time period where we have collocated MRMS and in situ probe data. For both legs and both B20 retrieval methods, the optimal α is generally about 0.2 g cm^{-3} mm and $\overline{\varphi} \approx 0.2$ for periods of dry ice. For periods of supercooled liquid droplets such as 1520 and 1531 UTC (see Fig. 6), both α and $\overline{\varphi}$ increase in accordance with the effects of riming.

Unlike α and $\overline{\varphi}$, σ has no direct information content and the marginal distributions of σ at each time period is roughly uniform from 0° to 40°. The optimal μ values for leg 1 and leg 2 are qualitatively similar to those estimated from the P3-derived incomplete gamma distribution (Fig. 7). In particular, similar to the in situ measurements, the optimal μ values are predominantly positive during leg 1 and mimic the general increase in positivity during the latter periods of leg 2. While both $\mu = 0$ and variable-μ B20 retrievals are capable of retrieving values of $D_{m,\max}$, N_t, and IWC that are consistent with in situ observations, the inclusion of μ is capable of improving N_t and IWC retrievals especially during these periods of positive μ.

Correlations between each variable are shown in Fig. 13 where each set of joint posterior distributions corresponds to the collated optimal parameters for the μ-dependent B20 retrievals for each 5 s time period. As shown in this figure, each pair of parameters is roughly related to one another in the form of

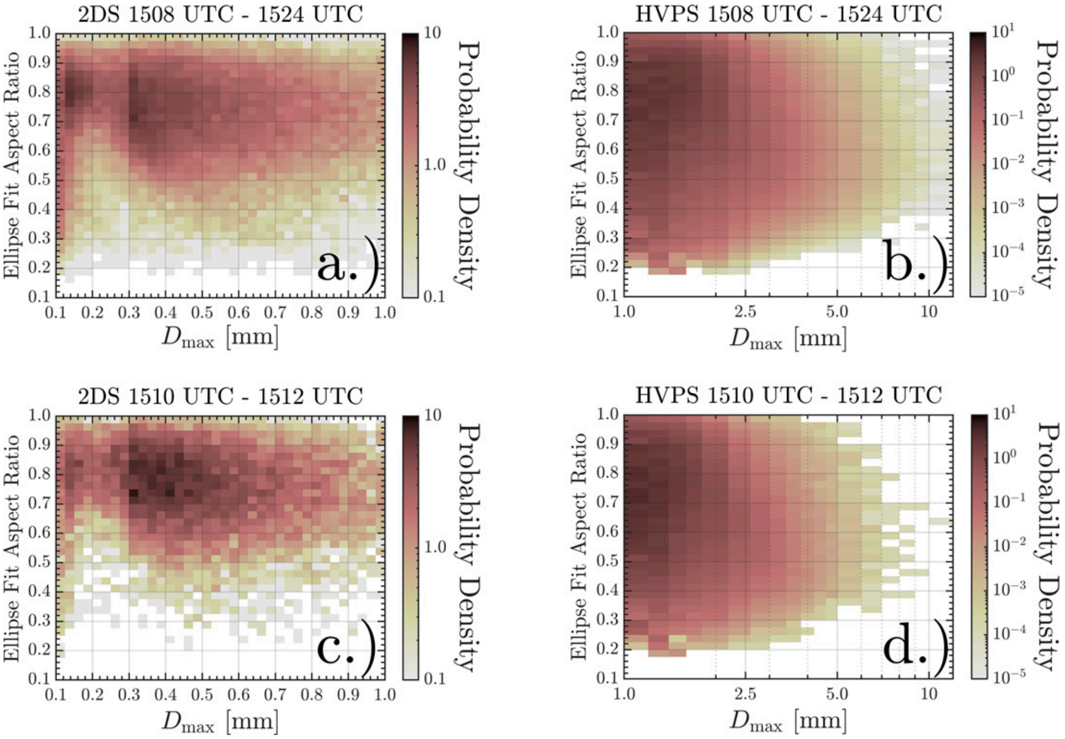

FIG. 9. Observed leg-1 joint probability distributions of ellipse fit aspect ratios and maximum dimension for ice particles viewed from the horizontal plane: (a) 2DS probe for entire leg, (b) HVPS probe for entire leg, (c) 2DS probe for 1510–1512 UTC, and (d) HVPS probe for 1510–1512 UTC. Only particles that are fully within the probe sampling volumes are included.

power laws. In particular, the correlations between $\overline{\varphi}$ and σ are due to the effects each has on F_s; F_s maximizes for low aspect ratios and low σ values. However, $D_{m,\max}$ depends inversely on α and implicitly on $\overline{\varphi}$ but not σ. Therefore, for a given Z and K_{dp} pair, optimal lower values of σ will map to lower values of α and higher values of $\overline{\varphi}$, whereas higher values of σ will map to higher values of α and lower values of $\overline{\varphi}$. Remarkably, the joint distributions in Fig. 13 are very consistent between leg 1 and leg 2. The main difference between leg 1 and leg 2 results from periods of significant supercooled liquid droplets at the beginning of leg 2. During these supercooled liquid droplet periods, α is very high. Overall, both legs show that aspect ratios are generally low and less than 0.4 and are positively correlated with α. The μ is negatively correlated with both α and $\overline{\varphi}$ for both legs where leg 2 has predominantly more negative μ values than leg 1.

6. Discussion

a. What caused each dendritic growth layer K_{dp} and Z_{DR} enhancement?

The collocated MRMS variables with in situ measurements shown in section 5a provide a complex picture for inferring which physical mechanism caused each K_{dp} and Z_{DR} enhancement in leg 1. Here, we attempt to explain which physical mechanisms could plausibly explain each set of observations for each enhancement region and how each mechanism relates to previous theories and hypotheses.

For the first K_{dp} and Z_{DR} peak at 1510 UTC, Fig. 8 clearly suggests that each enhancement is in some way related to a local enhancement in N_t. However, it is not entirely clear which physical mechanism corresponds to such an N_t enhancement. A local increase in the number of dendrites or planar crystals, as suggested by studies such as Kennedy and Rutledge (2011), Schrom et al. (2015), and Schrom (2018), provides perhaps the most straightforward explanation. However, the 3V-CPIview habit classifications (Fig. 6) do not suggest a prevalence of such particles at any portion of the flight, and the majority of particles tend to rather be irregular. Secondary ice production processes such as rime splintering represent another possibility. However, the lack of supercooled liquid droplets and the colder temperatures during leg 1 do not suggest any rime splintering. Another secondary ice production mechanism, collisional breakup of ice particles, represents a better possible explanation. A laboratory experiment by Lo (1983) suggests that fragment sizes of ice–ice collisions are approximately exponentially distributed where a majority of fragments (for collisions of particles 3 mm or larger) have sizes less than 0.6 mm. These fragment sizes are somewhat consistent with the 0.5-mm particles that primarily account for the N_t enhancement at 1510 UTC. Another laboratory study by Vardiman (1978) illustrates that light-to-moderately rimed spatial planar crystals, such as those observed in the current study, were the most efficient at producing fragments. However, Vardiman (1978) also found that such breakup required heavily rimed particles or graupel to produce such fragments. Thus, it is

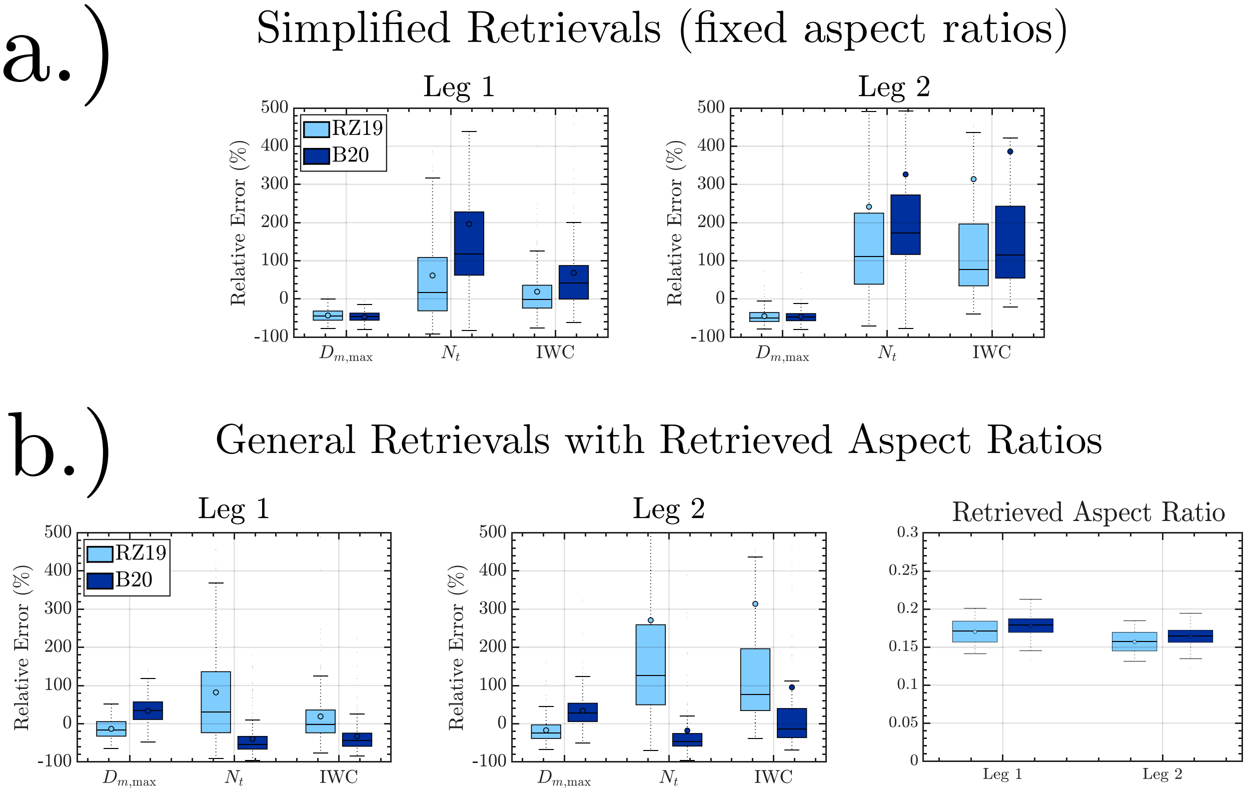

FIG. 10. Box-and-whisker plots of $D_{m,\max}$, N_t, and IWC relative errors for legs 1 (1508–1524 UTC) and 2 (1530–1551 UTC) using the simplified retrieval equations from RZ19 and B20 (see Table 1). Circles represent the distribution mean, and horizontal black lines represent distribution medians. Boxes encompass the 25th–75th interquartile range, and whiskers represent the smallest and largest data values within 1.5 times the interquartile range.

unclear whether secondary ice from collisional breakup could even efficiently take place for the first K_{dp} and Z_{DR} peak given the lack of observed rimed particles and supercooled liquid droplets. Some in situ studies such as Lo and Passarelli (1982) have, however, emphasized that such rimed particles are not required for breakup to occur. Theoretical studies such as Phillips et al. (2017) have highlighted the importance of ice–ice collisions yet some researchers such as Korolev and Leisner (2020) have questioned the reliability of such theory in the context of known artificial shattering issues induced by cloud probes and differences in laboratory setups for the few experiments that do exist. Considering the apparent correlation between the increase in N_t with increases in K_{dp} and Z_{DR} for the first peak, we hypothesize that either ice–ice collisional breakup or a seeder–feeder process such as that proposed by Moisseev et al. (2015) most likely explains the polarimetric enhancements at 1510 UTC.

For the second K_{dp} and Z_{DR} peak at about 1520 UTC, in situ probe data illustrates that supercooled liquid droplets were present (Fig. 6). Riming therefore provides a possible explanation for the second Z_{DR} and K_{dp} peak. Riming would naturally increase the density of ice particles, which, in turn, would enhance the effect anisotropic particles have on K_{dp} and Z_{DR} measurements. Particles at 1520 UTC were also generally larger than at 1510 UTC as indicated by $D_{m,\max} \approx 3.0$ mm values as compared with $D_{m,\max} \approx 2.0$ mm at 1510 UTC (Fig. 7). As indicated in the reflectivity time–height profile for leg 1 (Fig. 5), cloud heights were generally lower at 1520 UTC than at 1510 UTC. As suggested by Griffin et al. (2018) and briefly described in section 5a, the lower and warmer cloud top at 1520 UTC likely led to fewer large aggregates that usually tend to mute Z_{DR} in the dendritic growth layer. Large anisotropic crystals (as observed in some of the 2DS images) within these shallower cloud systems could therefore contribute more to Z_{DR} and K_{dp} than for colder clouds with higher cloud tops. This also explains why Z_{DR} was larger whereas K_{dp} was smaller for the second peak than for the first. However, unlike in Griffin et al. (2018), Z_{DR} and K_{dp} are clearly correlated, rather than anticorrelated. Also, unlike in Griffin et al. (2018), it does not appear that hexagonal plates were the primary cause of the second enhancement region. Thus, our best explanation for the cause of the second Z_{DR} and K_{dp} enhancement region at 1520 UTC is based on the combination of 1) riming affecting particle density, 2) the presence of a few large, anisotropic particles, and 3) a lower cloud top that limits the number of large aggregates and, in turn, reduces the Z_{DR} masking effect common for colder clouds.

b. *What are the true intrinsic ice particle aspect ratios?*

While MRMS retrievals seemingly require low aspect ratios ($\overline{\varphi} \approx 0.2$) to appropriately match observations as shown in Figs. 10, 12 and 13, fit aspect ratio observations (Fig. 9) and

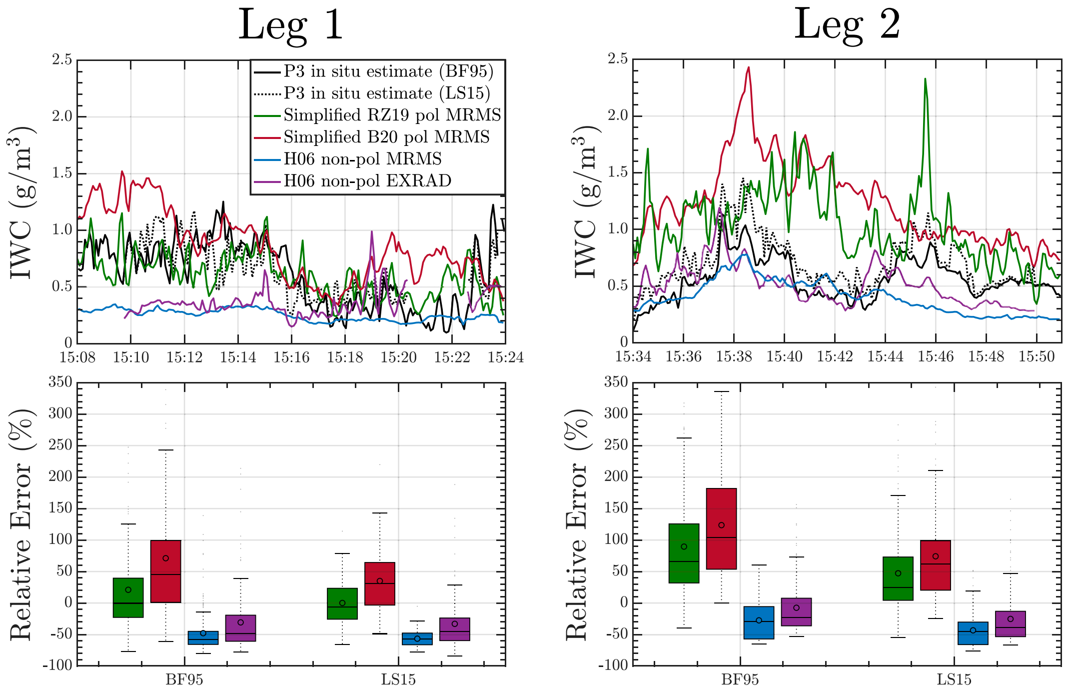

FIG. 11. (top) Comparison of bootstrap IWC retrievals following RZ19 (green; simplified RZ19), B20 (red; simplified B20), and H06 using the MRMS bootstraps (blue) and EXRAD reflectivity (purple) with two PSD estimates obtained from the P3 aircraft for legs (left) 1 and (right) 2. (bottom) IWC relative error boxplots for each leg using both BF95 and LS15 IWC estimates. Boxplots have the same statistical meanings as in Fig. 10.

habit classifications (Fig. 6) suggest instead that ice particles were much more spherical. Could low-aspect-ratio particles, in some way, explain the in situ observations despite the predominantly irregular particle types and high projected ellipse fit aspect ratios? Or, alternatively, are more spherical, but irregular, shapes necessary to explain these in situ observations?

To help reconcile this paradox, we perform idealized simulations of rotating and projecting oblate spheroids (mimicking low-aspect-ratio, planar crystals) and triaxial ellipsoids (mimicking various "irregular" particles) under various aspect ratio and orientation assumptions. This allows us to investigate which combinations of ice particle shapes and orientations could explain the in situ projection observations as shown in Fig. 9. The results of such an analysis are shown in Fig. 14 for oblate spheroids with aspect ratios of 0.2 (green, purple, and cyan lines), which are symbolic of $\overline{\varphi}$ retrievals as well as various triaxial ellipsoids (red lines) defined by bivariate beta distributions of two aspect ratios: $\varphi_{ba} = b/a$ and $\varphi_{ca} = c/a$ ($\varphi_{cb} \equiv c/b$). These tests and their orientation distributions are described in Table 2 and are shown alongside the computed distributions for both the vertically pointing and horizontally pointing HVPS instruments. In particular, the ellipse orientation angles are quasi-uniformly distributed but with slightly more counts at 0° and 90°, yielding a concave shape. To yield this type of 2D orientation distribution, the 3D orientation distribution must also similarly permit a concave shape. Therefore, we choose an orientation distribution similar to an arcsine distribution on the interval 0–1 and perform the transformation $u = \sin^2\theta$. Figure 14 shows that both the oblate spheroid (green lines) and triaxial ellipsoid tests (red lines) can capture the general shape of the 2D projection ellipse angle distributions. However, the distributions of oblate spheroid 2D projected ellipse aspect ratios do not exhibit the same shape as the observations but instead peak at the actual spheroid aspect ratio and tail off toward unity for both the horizontally and vertically oriented views. Triaxial ellipsoids with the quasi-arcsine orientations (solid red lines) can explain both distributions of observed 2D aspect ratios and ellipse orientation angles. Random orientations (dotted red lines) are qualitatively similar to the quasi-arcsine distribution with the exception that the 2D ellipse orientation distributions are uniform on the interval 0°–90°.

For $\varphi = 0.2$ oblate spheroids to yield the observed bell-shaped 2D projected aspect ratio distributions, the spheroids need to be canted such that their faces are preferentially pointed toward the imager as suggested by some of the 2DS particle images. As shown in Fig. 14, a Gaussian distribution for θ can approximate the aspect ratio distribution for one view (i.e., horizontal view) but not for the other view (purple lines). Normal distributions for all three Euler orientation angles (cyan lines) can produce similar bell-shaped aspect ratio distributions to that of the observations but cannot capture the concave 2D ellipse orientation distribution. As stated before, retrievals are thought to potentially introduce intrinsic aspect ratio uncertainties up to 0.2 (Matrosov 2020). Despite this uncertainty, the inability for oriented oblate spheroids to produce the correct *distributions* of projected ellipse aspect ratios and orientations suggests that the observed ice particle shapes were more representative of irregular shapes

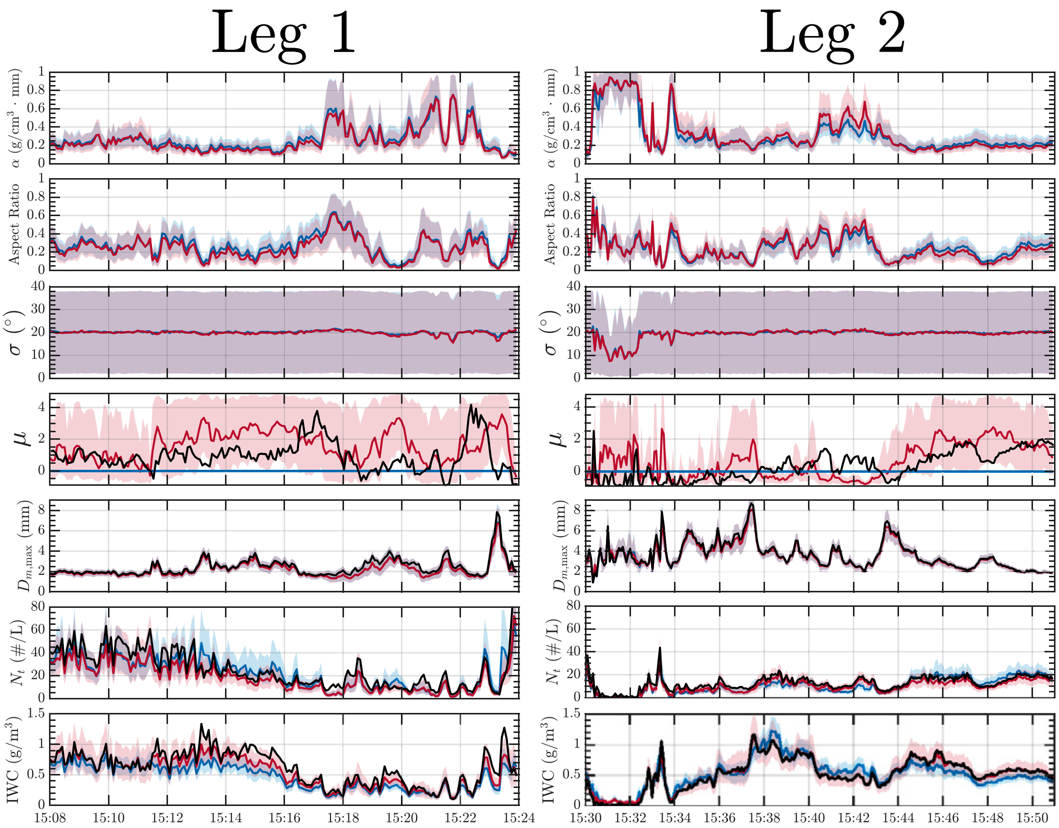

FIG. 12. B20 parameters and corresponding retrievals for (from top to bottom): α, $\overline{\varphi}$, σ, μ, $D_{m,\mathrm{max}}$, N_t, and IWC for (left) leg 1 and (bottom) leg 2. The MCMC algorithm was used for each 5-s time period for the simplified B20 retrieval (blue; $\mu = 0$) and the general B20 retrieval (red). Black lines represent the in situ measurements from Fig. 7. Shaded regions represent the 5th–95th percentiles of parameters and retrievals from 10 000 random samples of the posterior B20 parameter distributions, and solid lines correspond to the arithmetic mean of these posterior samples.

characteristic of the triaxial ellipsoid tests in Fig. 14. This is also consistent with CPI habit classifications (Fig. 6), which indicate that irregular particles, rather than hexagonal plates or dendrites, dominate ice habits for all periods.

This projection behavior for oblate spheroids is confirmed in Fig. 15, which shows a side-by-side comparison of example 2DS images of dendrites and planar particles with the 2DS-derived projected aspect ratio and ellipse orientation distributions for each orthogonal 2DS probe view. Unlike the HVPS, the 2DS-H and 2DS-V projections have partially overlapping sampling volumes and thus the 2DS-H and 2DS-V distributions more-or-less represent the same particles being viewed along flight (2DS-H) and along the particle fall speed direction (2DS-V). Moreover, an additional Monte Carlo oblate spheroid projection test (test 7 in Table 2) is performed to compare both the resulting distributions and the example projection images. Here, oblate spheroid aspect ratios are randomly chosen between 0.1 and 0.3 to mimic potential observed dendrites and planar crystals consistent with retrievals using CDR_p. Similar to Fig. 14, low-aspect-ratio oblate spheroids can explain the observed 2D ellipse orientation distributions if they exhibit some beta-like canting angle distribution with their major dimension randomly oriented in the horizontal plane. As in Fig. 14, the resulting projected aspect ratio distribution peaks at lower values than observed. Example 2DS images of dendrites and planar crystals in Fig. 15 are qualitatively consistent with the Monte Carlo simulated oblate spheroids: both viewing directions show examples where the basal facet of the planar crystals are tilted away from the imager as well as facing toward the imager. This further illustrates that a mixture of a low number concentration of large dendrites and a higher concentration of higher-aspect-ratio, irregular, and aggregate particles with triaxial shapes can explain the 2DS and HVPS observations.

c. *MRMS retrieval uncertainties and biases*

One reason for a possible underestimation of radar-based retrieved particle aspect ratios are potential biases in the estimates of CDR_p, which are based on averaged values of Z_{dr} and ρ_{hv} [Eq. (5)] as reported by the MRMS system. Previous studies (Matrosov et al. 2017; Matrosov 2020) with radar measurements at closer ranges [thus generally with high signal-to-noise ratios (SNR)] indicated that minimal CDR_p values corresponding to quasi-spherical particles with larger aspect ratios are around −27 dB. High minimal CDR_p values are generally expected

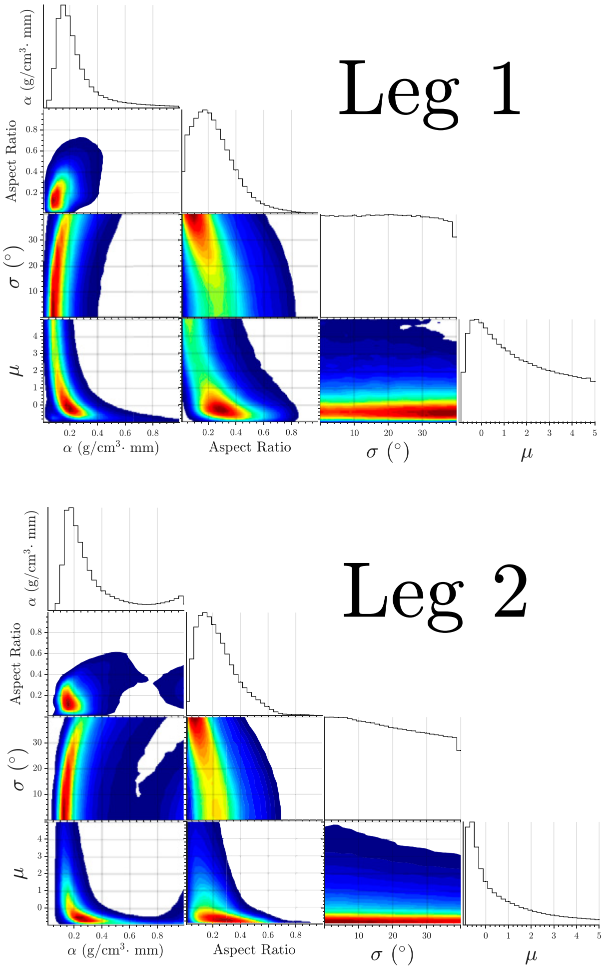

FIG. 13. Combined posterior parameter distributions for generalized B20 retrievals using MCMC methodology for (top) leg 1 and (bottom) leg 2.

from particles with lower aspect ratios (Matrosov et al. 2020). CDR_p estimates are quite sensitive to biases in Z_{dr} and ρ_{hv} data. Underestimation of ρ_{hv} values at low SNRs by about 0.006 could explain an approximate −4 dB in minimal CDR_p values. Additionally, radar-based ice particle aspect ratio retrievals are weighted by larger particles because of a general D^n dependence of radar variables as shown in Eq. (A9). As a result of this dependence, particle mixtures (e.g., more numerous smaller quasi-spherical particles and larger dendritic particles) will yield biased retrieved aspect ratios relative to a simple mean aspect ratio value.

The MRMS spatiotemporal resolution could also explain some of the observed discrepancies between the in situ observed $D_{m,\max}$ peaks as shown in Fig. 7 and the retrieved $D_{m,\max}$ from the results section (section 5). Because the $D_{m,\max}$ peaks are rather sharp, it is possible for the MRMS collocated time series to not properly resolve these regions of enhanced Z responsible for these peaks. Figure 16 shows evidence for this hypothesis by comparing the collocated MRMS reflectivity and the airborne ER2 EXRAD X-band reflectivity with the P3-observed $D_{m,\max}$. Figure 16 shows that various $D_{m,\max}$ peaks (e.g., 1515, 1519, 1537, and 1544 UTC) correlate with the ER2 EXRAD X-band radar reflectivity peaks, whereas the MRMS S-band radar bootstrap observations are not able to resolve these peaks. Furthermore, the MRMS Z is generally biased toward lower values than the EXRAD observations. This suggests that some of the biases in the retrievals (i.e., low $D_{m,\max}$ and high N_t) could result from a low bias in Z from the MRMS. The 2-min MRMS Z (blue) are very similar to the 10-min MRMS Z except from 1514 to 1521 UTC and from 1534 to 1538 UTC where the 2-min data has slightly lower reflectivity values. This suggests that the majority of the discrepancy between the EXRAD and MRMS comes from spatial uncertainties rather than temporal uncertainties.

7. Summary and conclusions

This study shows that current PSD and aspect ratio dual-polarization radar retrieval methodologies for ice particles in a winter storm can produce similar values and behaviors to those derived explicitly from in situ observations in the mean. However, there are several important limitations, uncertainties, and caveats that heavily influence these retrieved PSD and aspect ratio variables. Using simplified retrieval equations that assume typical values of $\overline{\varphi} \approx 0.6-0.8$ (e.g., those used in RZ19 and B20) generally led to underestimation of retrieved $D_{m,\max}$ by approximately 50% and overestimation of retrieved N_t by approximately 100%, relative to the in situ measurements for both legs. While median relative errors for RZ19 N_t for leg 1 were reasonably low (+17%), the interquartile range spanned a large range (approximately from −25% to +100%). These N_t errors expanded for leg 2 where the median relative errors were approximately +100% for the entire leg relative to in situ measurements. RZ19 IWC and N_t retrievals had the lowest relative errors within the dendritic growth layer during leg 1, whereas B20 IWC retrievals with CDR_p aspect ratio retrievals had the lowest relative errors for leg 2. Aspect ratio retrievals using the methodology of Matrosov et al. (2020) yielded low values in the dendritic growth layer ($0.1 \leq \overline{\varphi} \leq 0.2$). Using these low aspect ratios in retrievals of $D_{m,\max}$ counteracts the generally low $D_{m,\max}$ bias relative to observations through the conversion of equivolume diameter to maximum dimension [Eq. (4)]. Optimal aspect ratios using the B20 retrievals from an MCMC algorithm (Fig. 13) also suggests the need for these low aspect ratios. However, these low aspect-ratio values were inconsistent with in situ observations (Fig. 9).

Some discrepancy between the retrieved particle aspect ratios and their in situ estimates necessarily resulted from discrepancies between the radar retrievals that represent intrinsic or 3D mean aspect ratio values and in situ ellipse fit data that were derived from 2D projections. Thus, some planar particle projections will have artificially large 2D ellipse fit aspect ratios because of their quasi-random orientations within the 2DS and HVPS sample volumes. However, numerical simulations (Figs. 14 and 15) showed that low-aspect-ratio planar particles cannot simultaneously match the observed distribution of 2D ellipse orientation angles and aspect ratios for both horizontally oriented and vertically oriented in situ cloud probes. To match the observed

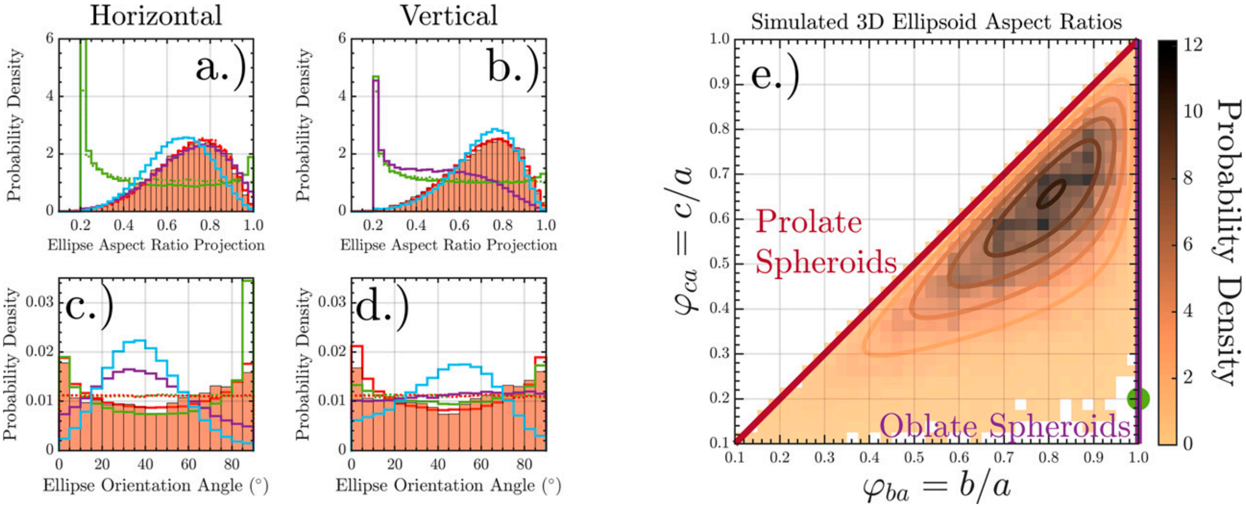

FIG. 14. Leg 1 probability density comparison of observed ellipse projections from the P3 HVPS instrument (shaded histograms) and Monte Carlo simulated estimates of various ellipsoids (colored lines) assuming various orientation distributions for test conditions given in Table 2: (a) Horizontal view ellipse aspect ratio 2D projection distributions. (b) Vertical view ellipse aspect ratio 2D projection distributions. (c) Horizontal view ellipse orientation 2D projection distributions. (d) Vertical view ellipse orientation 2D projection distributions. Also shown is the (e) Monte Carlo simulated joint distribution (shaded) of triaxial ellipsoid aspect ratios used for projection analysis with the analytic representation (contours). The oblate spheroid aspect ratio in the projection analysis is represented with a green circle at $\varphi_{ba} = 1.0$ and $\varphi_{cb} = 0.2$.

distribution of 2D ellipse angles for both probe orientations, planar particles must be quasi-randomly oriented as might be expected from turbulence generated within and around in situ cloud probes. However, these orientations necessarily lead to a bimodal distribution of 2D ellipse aspect ratios rather than the observed unimodal distribution. More likely, MRMS uncertainties and retrieval assumptions are responsible for the observed discrepancies. In particular, a comparison between the collocated MRMS reflectivity and that of the ER2 EXRAD radar and measurements of $D_{m,\max}$ taken from the P3 probes (Fig. 16) illustrates that the MRMS cannot resolve local Z peaks responsible for enhanced $D_{m,\max}$ values due to the MRMS horizontal resolution. Another source of discrepancy between retrievals of aspect ratios and their 2D projections is that radar-based retrievals are weighted by larger dendritic-type particles due to reflectivity dependence as approximately D^4, while in situ estimates represent simple mean values, which could be dominated by smaller quasi-spherical particles.

The ability to collocate polarimetric radar variables directly with in situ aircraft data has also allowed us to investigate the various underlying causes of the often-discussed dendritic growth layer K_{dp} and Z_{DR} enhancement regions associated with the onset of aggregation (Kennedy and Rutledge 2011; Moisseev et al. 2015). In situ aircraft and satellite observations

TABLE 2. Ellipsoid test parameters used in Figs. 14 and 15, where $a \geq b \geq c$ are semiaxis lengths with aspect ratios: $\varphi_{ba} \equiv b/a$, $\varphi_{ca} \equiv c/a$, and $\varphi_{cb} \equiv c/b$; $B(a, b)$ is the beta function; $K(x)$ is the complete elliptic integral of the first kind; $0 \leq \phi(\psi) \leq 2\pi$; $0 \leq \theta \leq \pi/2$; $\mathcal{N}_1$ is a normal distribution with $\mu_r = 60°$ and $\sigma_r = 17°$; $\mathcal{N}_2$ is a normal distribution with $\mu_r = 55°$ and $\sigma_r = 14°$; and $\tilde{n}(\varphi_{ba}, \varphi_{ca})$ is a bivariate beta distribution (Dunnavan et al. 2019) characterized by $\overline{\varphi}_{ba} = \overline{\varphi}_{cb} = 0.75$ shown in Fig. 14e.

Test	Color/line style	Orientation	$p(\phi)$	$p(\theta)$	$p(\psi)$	φ_{ba}	φ_{cb}
			Figure 14				
1	Green/solid	Quasi-arcsine	$(2\pi)^{-1}$	$\frac{\cos^{-1/2}\theta}{\sqrt{2}K(1/2)}$	$(2\pi)^{-1}$	1.0	0.2
2	Green/dotted	Random	$(2\pi)^{-1}$	$\sin\theta$	$(2\pi)^{-1}$	1.0	0.2
3	Purple/solid	Random/Gaussian	$(2\pi)^{-1}$	$\mathcal{N}_1$	$(2\pi)^{-1}$	1.0	0.2
4	Cyan/solid	Gaussian	$\mathcal{N}_2$	$\mathcal{N}_2$	$\mathcal{N}_2$	1.0	0.2
5	Red/solid	Quasi-arcsine	$(2\pi)^{-1}$	$\frac{\cos^{-1/2}\theta}{\sqrt{2}K(1/2)}$	$(2\pi)^{-1}$	$\tilde{n}(\varphi_{ba}, \varphi_{ca})$	
6	Red/dotted	Random	$(2\pi)^{-1}$	$\sin\theta$	$(2\pi)^{-1}$	$\tilde{n}(\varphi_{ba}, \varphi_{ca})$	
			Figure 15				
7	Blue/solid	Beta quasi-random	$(2\pi)^{-1}$	$\frac{2\sqrt[4]{\tan\theta\sin\theta}}{B(3/4, 3/8)}$	$(2\pi)^{-1}$	1.0	0.1–0.3

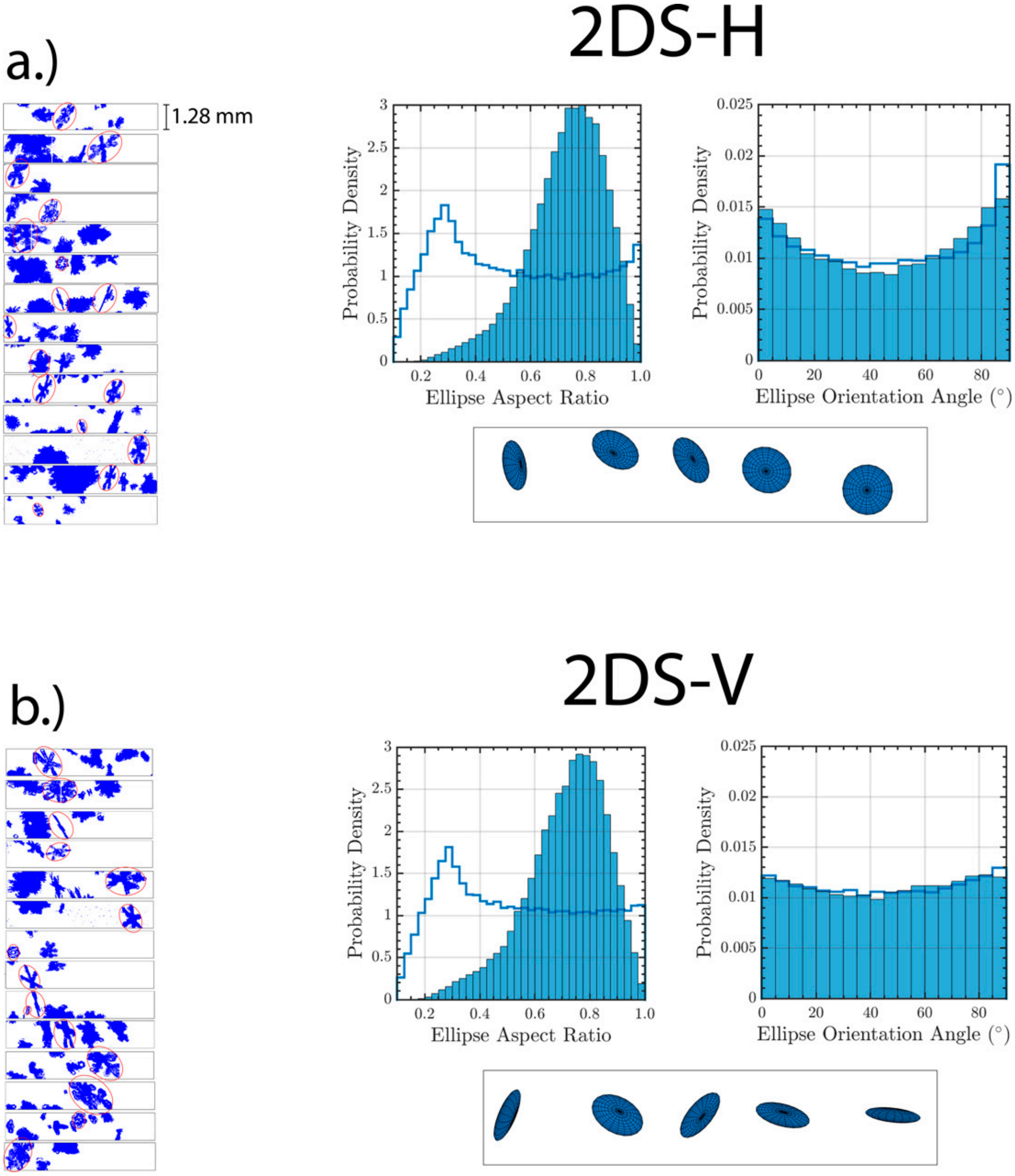

FIG. 15. (left) 2DS images of dendrites and planar particles taken during leg 1. Clear examples of dendrites and planar particles are circled in red. (right) Comparison of 2DS distributions of 2D ellipse fit aspect ratios and ellipse orientation angles (shaded histograms) and analogous distributions of beta-oriented (see Table 2) Monte Carlo simulated 3D oblate spheroids with random aspect ratios between 0.1 and 0.3 (lines). Below each distribution plot are 5 random samples of oblate spheroid views assuming the (a) 2DS-H and (b) 2DS-V orthogonal viewing angles. The 2DS-H and 2DS-V share the same sampling volume.

(Fig. 6) illustrate that both dry ice particles and mixtures of ice particles and supercooled liquid droplets can exist in these enhancement regions. The first K_{dp} and Z_{DR} peak occurred in a region with little to no observed supercooled liquid droplets and no noticeable change in ice particle habit (Fig. 6). Low temperatures ($T \approx -16°\mathrm{C}$) and lack of supercooled liquid droplets suggests that rime splintering was not active in this region. However, this first peak did show elevated values of N_t, which suggests that increases in N_t from irregular crystals drove enhancements in both K_{dp} and Z_{DR}. It is possible that secondary ice production such as ice–ice collisional breakup could plausibly explain this local increase in N_t. However, various studies present conflicting views on the need for rimed particles for such breakup to occur as well as the reliability of previous experimentation for understanding the ice–ice collisional breakup process (Lo and Passarelli 1982; Vardiman 1978;

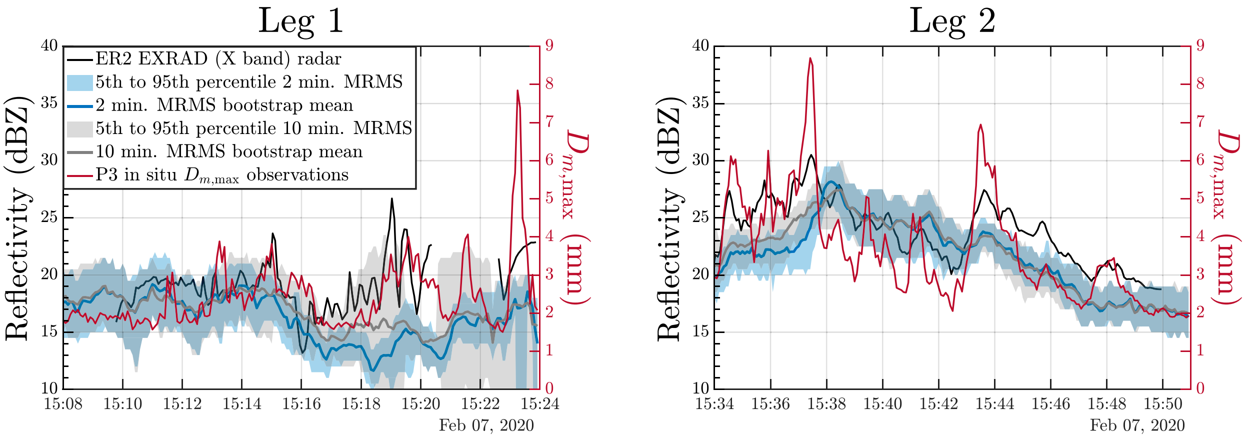

FIG. 16. Time series of reflectivity for the ER2 EXRAD X-band radar (black lines) and the 2-min (blue) and 10-min (gray) MRMS S-band radar along with estimates of $D_{m,\max}$ from the P3 aircraft. For the EXRAD reflectivity, time periods are not included if the horizontal difference in distance between the ER2 and P3 is greater than 4 km.

Phillips et al. 2017; Korolev and Leisner 2020). On the other hand, in situ probe data illustrate that supercooled liquid droplets were present during the second K_{dp} and Z_{DR} peak. Higher $D_{m,\max}$ and lower N_t values at 1520 UTC than at 1510 UTC suggest that large, anisotropic particles at 1520 UTC had a larger impact on K_{dp} and Z_{DR} than the smaller, irregular particles. Overall, despite similar polarimetric radar variable values and tendencies, in situ observations in these regions suggest that IWC, N_t, and $D_{m,\max}$ in these regions can be vastly different. It is clear that some of these differences are attributable to differences in particle characteristics related to particle shape ($\overline{\varphi}$), orientation (σ), and density (α). As a result, future retrieval methods will need to incorporate different strategies or assumed parameter values (i.e., α, σ, and $\overline{\varphi}$) for these different types of K_{dp} and Z_{DR} enhancement regions.

Acknowledgments. The authors are very thankful for the NSSL MRMS team and, in particular Andrew Osborne, who graciously provided us with the MRMS datasets used for this study. We are also tremendously grateful to the IMPACTS team that collected a comprehensive in situ and remote sensing dataset enabling this study. In particular, we thank Gerry Heymsfield for his input into this study with regard to the ER2 EXRAD data. The authors also thank Peter Brechner (University of Oklahoma School of Meteorology) for his willingness to provide the incomplete gamma fitting routine used in this work as well as Paul Lawson and Sarah Woods (SPEC, Inc.) for providing us with the 3V-CPIview software we used for CPI habit classification. The authors thank the three reviewers of this paper who helped to greatly improve this study with their feedback and suggestions. The IMPACTS project was funded by the NASA Earth Venture Suborbital-3 (EVS-3) program and managed by the Earth System Science Pathfinder (ESSP) Program Office. Funding for this study was provided by NOAA/Office of Oceanic and Atmospheric Research under NOAA–University of Oklahoma Cooperative Agreement NA21OAR4320204, U.S. Department of Commerce, by the U.S. Department of Energy's Atmospheric Science Program Atmospheric System Research, an Office of Science, Office of Biological and Environmental Research program under DOE ASR Grant DE-SC0018967, by NASA Grant 80NSSC19K0399, and by NSF Grant 1841246.

Data availability statement. Archival MRMS data used in this paper were requested directly from the NSSL MRMS team. The IMPACTS EXRAD, CPI, RICE, FCDP, 2DS, and HVPS probes used within this analysis are available online from the NASA EOSDIS Global Hydrology Resource Center Distributed Activate Archive Center (https://doi.org/10.5067/IMPACTS/DATA101). UND particle probe data can be found online (https://doi.org/10.5067/IMPACTS/MULTIPLE/DATA101; Delene 2022). Aircraft data were processed using the Airborne Data Processing and Analysis package (Delene 2011), the University of Illinois/Oklahoma Optical Array Probe (OAP) Processing Software (https://doi.org/10.5281/zenodo.1285969), and 3V-CPIview software (SPEC, Inc.; http://www.specinc.com/3v-cpi-combo).

APPENDIX

Radar Retrieval Methodology

Four radar variables (Z, Z_{DR}, K_{dp}, and ρ_{hv}) can be used as constraints to estimate up to four PSD or particle property parameters (RZ19). We utilize several simplifications and approximations for the shape, density, and dielectric properties of the snow particles and we exploit integral properties of an a priori defined PSD. First, we assume that the ice/snow particles are described as oblate spheroids with aspect ratios of $\varphi \equiv b/a$, where a and b are the semimajor and semiminor axis lengths, respectively. We assume that these spheroids have effective densities that decrease as D^{-1}, where D is the equivolume diameter in units of millimeters and $D = \overline{\varphi}^{1/3} D_{\max}$, where $D_{\max} = 2a$ is the particle maximum dimension. This inverse size dependence for density has been observationally documented in a variety of studies (e.g., Magono and Nakamura 1965; Mitchell et al. 1990; Heymsfield et al. 2004; Brandes et al. 2007; Tiira et al. 2016) for various definitions and bulk measures of size. This implies that

$$\rho_s = \alpha D^{-1}, \tag{A1}$$

where α (g cm^{-3} mm) is a density quantity that can vary depending on the degree of riming. Multiplying this density with particle volume describes particle masses m_s in units of grams:

$$m_s = \rho_s V_s = 0.001 \frac{\pi}{6} \alpha D^2. \tag{A2}$$

Forward and backward radar Rayleigh scattering amplitudes can be defined as follows:

$$f_{a,b} = f_{a,b}(0) = f_{a,b}(\pi) = \frac{\pi^2 D^3}{6\lambda^2} \xi_{a,b}, \tag{A3}$$

which contains the combined shape/dielectric factor

$$\xi_{a,b} = \frac{1}{L_{a,b} + \dfrac{1}{\varepsilon_s(D) - 1}}, \tag{A4}$$

where ε_s corresponds to the dielectric constant for ice/snow and $L_{a,b}$ represents oblate spheroid geometric factors along the associated a axis and b axis given by

$$L_b = \frac{1+\kappa^2}{\kappa^2}\left[1 - \frac{\arctan(\kappa)}{\kappa}\right] \quad \text{and} \tag{A5a}$$

$$L_a = \frac{1 - L_b}{2}, \tag{A5b}$$

and $\kappa = \sqrt{\varphi^{-2} - 1}$. For spherical inclusions, $\varepsilon_s(D) - 1$ can be described in terms of snow density (cf. Ryzhkov et al. 2011):

$$\varepsilon_s - 1 = 3 \frac{\rho_s}{\rho_i} K_i, \tag{A6}$$

where $K_i = (\varepsilon_i - 1)/(\varepsilon_i + 2)$, and $\varepsilon_i = 3.168 + 0.0089i$ is the dielectric constant for solid ice.

Equations for each radar variable are (cf. Ryzhkov et al. 1998, 2011)

$$Z_h = \frac{1}{9|K_w|^2} \int_{D=0}^{\infty} F_{z_h}(D) D^6 n(D)\, dD, \tag{A7a}$$

$$Z_v = \frac{1}{9|K_w|^2} \int_{D=0}^{\infty} F_{z_v}(D) D^6 n(D)\, dD, \tag{A7b}$$

$$Z_{\text{dp}} \equiv Z_h - Z_v = \frac{1}{9|K_w|^2} \int_{D=0}^{\infty} F_{z_{\text{dp}}}(D) D^6 n(D)\, dD, \tag{A7c}$$

$$K_{\text{dp}} = \frac{0.03\pi}{\lambda} \int_{D=0}^{\infty} F_{k_{\text{dp}}}(D) D^3 n(D)\, dD, \quad \text{and} \tag{A7d}$$

$$\rho_{\text{hv}} = \frac{1}{9|K_w|^2} \frac{\left| \int_{D=0}^{\infty} F_{\rho_{\text{hv}}}(D) D^6 n(D)\, dD \right|}{\sqrt{Z_h Z_v}}, \tag{A7e}$$

where $n(D)$ is the number distribution function, $Z_{\text{dr}} = Z_h/Z_v$ (linear units), λ is the radar wavelength in millimeters, and $|K_w|^2 = 0.93$ is the dielectric factor for liquid water. For radar retrieval purposes, the integral limits given in Eq. (A7) are from 0 to ∞, although it is expected that that there would naturally be a finite lower and upper equivolume diameter. The effective shape/density factors are given by

$$F_{z_h}(D) = |\xi_a(D)|^2 - 2\text{Re}\{\xi_a^*(D)[\xi_a(D) - \xi_b(D)]\}A_2 + |\xi_a(D) - \xi_b(D)|^2 A_4, \tag{A8a}$$

$$F_{z_v}(D) = |\xi_a(D)|^2 - 2\text{Re}\{\xi_a^*(D)[\xi_a(D) - \xi_b(D)]\}A_1 + |\xi_a(D) - \xi_b(D)|^2 A_3, \tag{A8b}$$

$$F_{z_{\text{dp}}}(D) = 2\text{Re}\{\xi_a^*(D)[\xi_a(D) - \xi_b(D)]\}(A_1 - A_2) + |\xi_a(D) - \xi_b(D)|^2 (A_4 - A_3), \tag{A8c}$$

$$F_{k_{\text{dp}}}(D) = \text{Re}[\xi_a(D) - \xi_b(D)]A_7, \quad \text{and} \tag{A8d}$$

$$F_{\rho_{\text{hv}}}(D) = |\xi_a(D)|^2 + |\xi_a(D) - \xi_b(D)|^2 A_5 - \xi_a^*(D)[\xi_a(D) - \xi_b(D)]A_1 - \xi_a(D)[\xi_a^*(D) - \xi_b^*(D)]A_2, \tag{A8e}$$

where $A_n = A_n(\sigma)$ are angular moments given in Ryzhkov et al. (2011) that depend upon the assumed canting angle standard deviation σ; σ for different particles is largely unknown in general, and orientation distributions might not necessarily be best represented by an axisymmetric Gaussian distribution. For example, orientation distributions derived from the Multi-Angle Snowflake Camera (MASC) by Garrett et al. (2015) and more recently by Fitch et al. (2021) suggest that the orientation mode, defined as the absolute value of the angle between the maximum dimension and the horizontal, is not 0° and depends upon wind speed. While the 2D orientation angle defined by Garrett et al. (2015) and Fitch et al. (2021) differs from the 3D orientation angles defined by Ryzhkov et al. (2011), the inconsistency in *modal* values suggests perhaps a more complicated orientation distribution than the axisymmetric Gaussian distribution used by Ryzhkov et al. (2011). However, it is expected that the *mean* 3D orientation angle (defined as the angle between the maximum dimension and the horizontal in the range from −90° to +90°) is approximately 0° because of the lack of observed depolarization effects in snow (Ryzhkov et al. 2002). While the ground-based measurements of Garrett et al. (2015), Fitch et al. (2021), and others inevitably introduce orientation uncertainty resulting from potential instrumental disturbances, the most recent efforts of Fitch et al. (2021) involved the use of double-fence shielding, which acts to diminish any potential instrumental disturbance. Despite these nuances, we elect to use the axisymmetric Gaussian convention and distribution by Ryzhkov et al. (2011) such that we can evaluate currently used retrieval equations.

Notice in Eq. (A1) that ρ_s becomes unphysically larger than the bulk density of ice for small sizes. As a result, the CDR$_p$ retrievals described in section 4c explicitly sets the upper limit of ρ_s to the bulk density of ice ρ_i for these small sizes. For the RZ19 and B20 retrieval methodologies, this inconsistency is ignored such that the retrievals can be expressed as simple formulas. Therefore, the following equations are specifically valid for sufficiently large D_m ($D_m > 1.0$ mm).

As shown in RZ19 and B20, when the density of particles is small, Eq. (A8) can be expanded as a Taylor series in powers of $|\varepsilon_s - 1|$ where the first term represents a simple power law (Ryzhkov et al. 1998; RZ19) in terms of D. Replacing each shape/density term in Eqs. (A7a), (A7c), and (A7d) with its power-law approximation allows for each radar variable to be represented as

$$Z_h = \frac{|K_i|^2}{|K_w|^2}\left(\frac{\alpha}{\rho_i}\right)^2 M_4, \tag{A9a}$$

$$Z_{\mathrm{dp}} = \frac{6|K_i|^3}{|K_w|^2}\left(\frac{\alpha}{\rho_i}\right)^3 F_s M_3, \quad \text{and} \tag{A9b}$$

$$K_{\mathrm{dp}} = \frac{0.27\pi}{\lambda}|K_i|^2\left(\frac{\alpha}{\rho_i}\right)^2 F_s M_1, \tag{A9c}$$

where $M_n \equiv \int D^n n(D)\,dD$ are the PSD moments (mm^n m^{-3}); $A_1 - A_2 = A_7$, $F_s \equiv A_7(L_b - L_a)$; $|K_i|$ and $|K_w|$ are the dielectric factors for solid ice and liquid water, respectively; and $\rho_i = 0.92$ g cm^{-3} is the bulk density of solid ice. We assume that the number distribution functions $n(D)$ are gamma distributions of the form

$$n(D) = \frac{(\mu+4)^{1+\mu}}{\Gamma(\mu+1)} N_t \frac{1}{D_m}\left(\frac{D}{D_m}\right)^{\mu} \exp\left[-\frac{(\mu+4)D}{D_m}\right], \tag{A10}$$

where moments of these distributions are

$$M_n = N_t(\mu+4)^{-n} D_m^n \frac{\Gamma(\mu+1+n)}{\Gamma(\mu+1)}, \tag{A11}$$

and $\Gamma(x)$ is the gamma function.

Using Eq. (A11) in Eq. (A9) allows for Z, Z_{dp}, and K_{dp} to be described in terms of the bulk parameters N_t and D_m. Therefore, two combinations of the equations in Eq. (A9) can be used to solve for N_t and D_m. IWC can then be solved by integrating Eq. (A2) with Eq. (A10) as follows:

$$\mathrm{IWC} = 0.001\frac{\pi}{6}\alpha M_2 = 0.001\frac{\pi}{6}N_t D_m^2 \frac{(\mu+2)(\mu+1)}{(\mu+4)^2}. \tag{A12}$$

RZ19 first uses the ratio $Z_{\mathrm{dp}}/K_{\mathrm{dp}}$ to calculate D_m. Dividing Eqs. (A9b) and (A9c) cancels N_t and allows for D_m to be expressed as

$$D_m = (\mu+4)\sqrt{\frac{0.27\pi|K_w|^2\rho_i Z_{\mathrm{dp}}}{6\lambda|K_i|(\mu+3)(\mu+2)\alpha K_{\mathrm{dp}}}}. \tag{A13}$$

The N_t can then be solved using any of the equations in Eq. (A9). For simplicity, we use Z_h, and the resulting expression for N_t is

$$N_t = \frac{36}{(0.27\pi)^2}\frac{1}{|K_w|^2}\lambda^2\frac{(\mu+3)(\mu+2)}{(\mu+4)(\mu+1)}K_{\mathrm{dp}}^2 Z_{\mathrm{dp}}^{-2} Z_h. \tag{A14}$$

IWC can be calculated with Eqs. (A12), (A13), and (A14):

$$\mathrm{IWC} = \frac{0.001\rho_i}{0.27|K_i|}\frac{\mu+2}{\mu+4}\lambda K_{\mathrm{dp}} Z_{\mathrm{dp}}^{-1} Z_h. \tag{A15}$$

For B20, D_m is solved using the ratio of K_{dp} [Eq. (A9c)] and Z_h [Eq. (A9a)]:

$$D_m = \left[\frac{0.27\pi|K_w|^2 F_s(\mu+4)^2 Z_h}{(\mu+3)(\mu+2)\lambda K_{\mathrm{dp}}}\right]^{1/3}. \tag{A16}$$

Again, N_t is solved using Z_h [Eq. (A9a)]:

$$N_t = \frac{|K_w|^2}{|K_i|^2}\left(\frac{\rho_i}{\alpha}\right)^2 (0.27\pi|K_w|^2 F_s)^{-4/3} \times \frac{[(\mu+4)(\mu+3)(\mu+2)]^{1/3}}{\mu+1}\lambda^{4/3}K_{\mathrm{dp}}^{4/3} Z_h^{-1/3}. \tag{A17}$$

Last, IWC is again calculated using Eq. (A12) and Eqs. (A16) and (A17):

$$\mathrm{IWC} = \frac{0.001\pi^{1/3}|K_w|^{2/3}\rho_i^2}{6(0.27F_s)^{2/3}|K_i|^2\alpha}\left[\frac{(\mu+2)^2}{(\mu+4)(\mu+3)}\right]^{1/3}\lambda^{2/3}K_{\mathrm{dp}}^{2/3} Z_h^{1/3}. \tag{A18}$$

Equations shown in Table 1 are simplified with $|K_w|^2 = 0.93$ and $|K_i| = 0.4195$.

REFERENCES

Andrić, J., M. R. Kumjian, D. S. Zrnić, J. M. Straka, and V. M. Melnikov, 2013: Polarimetric signatures above the melting layer in winter storms: An observational and modeling study. *J. Appl. Meteor. Climatol.*, **52**, 682–700, https://doi.org/10.1175/JAMC-D-12-028.1.

Auer, A. H., and D. L. Veal, 1970: The dimension of ice crystals in natural clouds. *J. Atmos. Sci.*, **27**, 919–926, https://doi.org/10.1175/1520-0469(1970)027<0919:TDOICI>2.0.CO;2.

Bailey, M. P., and J. Hallett, 2009: A comprehensive habit diagram for atmospheric ice crystals: Confirmation from the laboratory, AIRS II, and other field studies. *J. Atmos. Sci.*, **66**, 2888–2899, https://doi.org/10.1175/2009JAS2883.1.

Bechini, R., L. Baldini, and V. Chandrasekar, 2013: Polarimetric radar observations in the ice region of precipitating clouds at C-band and X-band radar frequencies. *J. Appl. Meteor. Climatol.*, **52**, 1147–1169, https://doi.org/10.1175/JAMC-D-12-055.1.

Brandes, E. A., K. Ikeda, G. Zhang, M. Schönhuber, and R. M. Rasmussen, 2007: A statistical and physical description of hydrometeor distributions in Colorado snowstorms using a video disdrometer. *J. Appl. Meteor. Climatol.*, **46**, 634–650, https://doi.org/10.1175/JAM2489.1.

Brown, P. R. A., and P. N. Francis, 1995: Improved measurements of the ice water content in cirrus using a total-water probe. *J. Atmos. Oceanic Technol.*, **12**, 410–414, https://doi.org/10.1175/1520-0426(1995)012<0410:IMOTIW>2.0.CO;2.

Bukovčić, P., A. Ryzhkov, D. Zrnić, and G. Zhang, 2018: Polarimetric radar relations for quantification of snow based on drisdrometer data. *J. Appl. Meteor. Climatol.*, **57**, 103–120, https://doi.org/10.1175/JAMC-D-17-0090.1.

——, ——, and ——, 2020: Polarimetric relations for snow estimation – radar verification. *J. Appl. Meteor. Climatol.*, **59**, 991–1009, https://doi.org/10.1175/JAMC-D-19-0140.1.

Chase, R. J., S. W. Nesbitt, and G. M. McFarquhar, 2021: A dual-frequency radar retrieval of two parameters of the snowfall particle size distribution using a neural network. *J. Appl. Meteor. Climatol.*, **60**, 341–359, https://doi.org/10.1175/JAMC-D-20-0177.1.

Chen, J.-P., and D. Lamb, 1994: The theoretical basis for the parameterization of ice crystal habit: Growth by vapor deposition. *J. Atmos. Sci.*, **51**, 1206–1222, https://doi.org/10.1175/1520-0469(1994)051<1206:TTBFTP>2.0.CO;2.

Cober, S. G., G. A. Isaac, A. V. Korolev, and J. W. Strapp, 2001: Assessing cloud-phase conditions. *J. Appl. Meteor.*, **40**, 1967–1983, https://doi.org/10.1175/1520-0450(2001)040<1967:ACPC>2.0.CO;2.

Delene, D. J., 2011: Airborne data processing and analysis software package. *Earth Sci. Inform.*, **4**, 29–44, https://doi.org/10.1007/s12145-010-0061-4.

——, 2022: UND Cloud Microphysics IMPACTS 2020, version 1. NASA Global Hydrometeorology Resource Center DAAC, accessed 21 February 2021, https://doi.org/10.5067/IMPACTS/MULTIPLE/DATA101.

Dunnavan, E. L., and Z. Jiang, 2019: A general method for estimating bulk 2d projections of ice particle shape: Theory and applications. *J. Atmos. Sci.*, **76**, 305–332, https://doi.org/10.1175/JAS-D-18-0177.1.

——, ——, J. Y. Harrington, J. Verlinde, K. Fitch, and T. J. Garrett, 2019: The shape and density evolution of snow aggregates. *J. Atmos. Sci.*, **76**, 3919–3940, https://doi.org/10.1175/JAS-D-19-0066.1.

Finlon, J. A., G. M. McFarquhar, S. W. Nesbitt, R. M. Rauber, H. Morrison, W. Wu, and P. Zhang, 2019: A novel approach for characterizing the variability in mass-dimension relationships: Results from MC3E. *Atmos. Chem. Phys.*, **19**, 3621–3643, https://doi.org/10.5194/acp-19-3621-2019.

Fitch, K. E., C. Hang, A. Talaei, and T. J. Garrett, 2021: Arctic observations and numerical simulations of surface wind effects on Multi-Angle Snowflake Camera measurements. *Atmos. Meas. Tech.*, **14**, 1127–1142, https://doi.org/10.5194/amt-14-1127-2021.

Garrett, T. J., S. E. Yuter, C. Fallgatter, K. Shukurko, S. R. Rhodes, and J. L. Endries, 2015: Orientations and aspect ratios of falling snow. *Geophys. Res. Lett.*, **42**, 4617–4622, https://doi.org/10.1002/2015GL064040.

Gärtner, B., and S. Schönherr, 1998: Exact primitives for smallest enclosing ellipses. *Inf. Process. Lett.*, **68**, 33–38, https://doi.org/10.1016/S0020-0190(98)00132-X.

Goodman, J., and J. Weare, 2010: Ensemble samplers with affine invariance. *Comm. App. Math. Comp. Sci.*, **5**, 65–80, https://doi.org/10.2140/camcos.2010.5.65.

Grazioli, J., G. Lloyd, L. Panziera, C. R. Hoyle, P. J. Connolly, J. Henneberger, and A. Berne, 2015: Polarimetric radar and in situ observations of riming and snowfall microphysics during CLACE 2014. *Atmos. Chem. Phys.*, **15**, 13 787–13 802, https://doi.org/10.5194/acp-15-13787-2015.

Griffin, E. M., T. J. Schuur, and A. V. Ryzhkov, 2018: A polarimetric analysis of ice microphysical processes in snow, using quasi-vertical profiles. *J. Appl. Meteor. Climatol.*, **57**, 31–50, https://doi.org/10.1175/JAMC-D-17-0033.1.

Grinsted, A., 2022: Ensemble MCMC sampler. Github, accessed 18 April 2022, https://github.com/grinsted/gwmcmc.

Harrington, J. Y., K. Sulia, and H. Morrison, 2013: A method for adaptive habit prediction in bulk microphysical models. Part II: Parcel model corroboration. *J. Atmos. Sci.*, **70**, 365–376, https://doi.org/10.1175/JAS-D-12-0152.1.

Heymsfield, A. J., A. Bansemer, C. Schmitt, C. Twohy, and M. R. Poellot, 2004: Effective ice particle densities derived from aircraft data. *J. Atmos. Sci.*, **61**, 982–1003, https://doi.org/10.1175/1520-0469(2004)061<0982:EIPDDF>2.0.CO;2.

Hogan, R. J., M. P. Mittermaier, and A. J. Illingworth, 2006: The retrieval of ice water content from radar reflectivity factor and temperature and its use in evaluating a mesoscale model. *J. Appl. Meteor. Climatol.*, **45**, 301–317, https://doi.org/10.1175/JAM2340.1.

——, L. Tian, P. R. A. Brown, C. D. Westbrook, A. J. Heymsfield, and J. D. Eastment, 2012: Radar scattering from ice aggregates using the horizontally aligned oblate spheroid approximation. *J. Appl. Meteor. Climatol.*, **51**, 655–671, https://doi.org/10.1175/JAMC-D-11-074.1.

Hu, J., D. Rosenfeld, Y. Zhu, X. Lu, and J. Carlin, 2021: Multichannel Imager Algorithm (MIA): A novel cloud-top phase classification algorithm. *Atmos. Res.*, **261**, 105767, https://doi.org/10.1016/j.atmosres.2021.105767.

Jensen, A. A., and J. Y. Harrington, 2015: Modeling ice crystal aspect ratio evolution during riming: A single-particle growth model. *J. Atmos. Sci.*, **72**, 2569–2590, https://doi.org/10.1175/JAS-D-14-0297.1.

Jiang, Z., M. Oue, J. Verlinde, E. E. Clothiaux, K. Aydin, G. Botta, and Y. Lu, 2017: What can we conclude about the real aspect ratios of ice particle aggregates from two-dimensional images? *J. Appl. Meteor. Climatol.*, **56**, 725–734, https://doi.org/10.1175/JAMC-D-16-0248.1.

Kennedy, P. C., and S. A. Rutledge, 2011: S-band dual-polarization radar observations of winter storms. *J. Appl. Meteor. Climatol.*, **50**, 844–858, https://doi.org/10.1175/2010JAMC2558.1.

King, W. D., 1985: Air flow and particle trajectories around aircraft fuselages. III: Extensions to particles of arbitrary shape. *J. Atmos. Oceanic Technol.*, **2**, 539–547, https://doi.org/10.1175/1520-0426(1985)002<0539:AFAPTA>2.0.CO;2.

——, 1986: Air flow and particle trajectories around aircraft fuselages. IV: Orientation of ice crystals. *J. Atmos. Oceanic Technol.*, **3**, 433–439, https://doi.org/10.1175/1520-0426(1986)003<0433:AFAPTA>2.0.CO;2.

Korolev, A., and G. Isaac, 2003: Roundness and aspect ratio of particles in ice clouds. *J. Atmos. Sci.*, **60**, 1795–1808, https://doi.org/10.1175/1520-0469(2003)060<1795:RAAROP>2.0.CO;2.

——, and T. Leisner, 2020: Review of experimental studies of secondary ice production. *Atmos. Chem. Phys.*, **20**, 11 767–11 797, https://doi.org/10.5194/acp-20-11767-2020.

Kumjian, M. R., and K. A. Lombardo, 2017: Insights into the evolving microphysical and kinematic structure of northeastern U.S. winter storms from dual-polarization Doppler radar. *Mon. Wea. Rev.*, **145**, 1033–1061, https://doi.org/10.1175/MWR-D-15-0451.1.

——, S. Mishra, S. E. Giangrande, T. Toto, A. V. Ryzhkov, and A. Bansemer, 2016: Polarimetric radar and aircraft observations of saggy bright bands during MC3E. *J. Geophys. Res. Atmos.*, **121**, 3584–3607, https://doi.org/10.1002/2015JD024446.

Lakshmanan, V., T. Smith, K. Hondl, G. J. Stumpf, and A. Witt, 2006: A real-time, three dimensional, rapidly updating, heterogeneous radar merger technique for reflectivity, velocity, and derived products. *Wea. Forecasting*, **21**, 802–823, https://doi.org/10.1175/WAF942.1.

Lamb, D., and W. D. Scott, 1972: Linear growth rates of ice crystals grown from the vapor phase. *J. Cryst. Growth*, **12**, 21–31, https://doi.org/10.1016/0022-0248(72)90333-8.

Leinonen, J., and W. Szyrmer, 2015: Radar signature of snowflake riming: A modeling study. *Earth Space Sci.*, **2**, 346–358, https://doi.org/10.1002/2015EA000102.

Lo, K. K., 1983: Growth processes of snow. Ph.D. thesis, Massachusetts Institute of Technology, 193 pp.

——, and R. E. Passarelli, 1982: The growth of snow in winter storms: An airborne observational study. *J. Atmos. Sci.*, **39**, 697–706, https://doi.org/10.1175/1520-0469(1982)039<0697:TGOSIW>2.0.CO;2.

Locatelli, J. D., and P. V. Hobbs, 1974: Fall speeds and masses of solid precipitation particles. *J. Geophys. Res.*, **79**, 2185–2197, https://doi.org/10.1029/JC079i015p02185.

Magono, C., and T. Nakamura, 1965: Aerodynamic studies of falling snowflakes. *J. Meteor. Soc. Japan*, **43**, 139–147, https://doi.org/10.2151/jmsj1965.43.3_139.

Matrosov, S. Y., 2020: Ice hydrometeor shape estimations using polarimetric operational and research radar measurements. *Atmosphere*, **11**, 97, https://doi.org/10.3390/atmos11010097.

——, C. G. Schmitt, M. Maahn, and G. de Boer, 2017: Atmospheric ice particle shape estimates from polarimetric radar measurements and in situ observations. *J. Atmos. Oceanic Technol.*, **34**, 2569–2587, https://doi.org/10.1175/JTECH-D-17-0111.1.

——, A. V. Ryzhkov, M. Maahn, and G. de Boer, 2020: Hydrometeor shape variability in snowfall as retrieved from polarimetric radar measurements. *J. Appl. Meteor. Climatol.*, **59**, 1503–1517, https://doi.org/10.1175/JAMC-D-20-0052.1.

McFarquhar, G. M., and R. A. Black, 2004: Observations of particle size and phase in tropical cyclones: Implications for mesoscale modeling of microphysical processes. *J. Atmos. Sci.*, **61**, 422–439, https://doi.org/10.1175/1520-0469(2004)061<0422:OOPSAP>2.0.CO;2.

——, A. J. Heymsfield, A. Macke, J. Iaquinta, and S. M. Aulenbach, 1999: Use of observed ice crystal sizes and shapes to calculate mean-scattering properties and multispectral radiances: CEPEX April 4, 1993 case study. *J. Geophys. Res.*, **104**, 31 763–31 779, https://doi.org/10.1029/1999JD900802.

——, G. Zhang, M. R. Poellot, G. L. Kok, R. McCoy, T. Tooman, A. Fridlind, and A. J. Heymsfield, 2007: Ice properties of single-layer stratocumulus during Mixed-Phase Arctic Cloud Experiment: 1. Observations. *J. Geophys. Res.*, **112**, D24201, https://doi.org/10.1029/2007JD008633.

——, T.-L. Hsieh, M. Freer, J. Mascio, and B. F. Jewett, 2015: The characterization of ice hydrometeor gamma size distributions as volumes in N_0–λ–μ phase space: Implications for microphysical process modeling. *J. Atmos. Sci.*, **72**, 892–909, https://doi.org/10.1175/JAS-D-14-0011.1.

McFarquhar, G. M., J. A. Finlon, D. M. Stechman, W. Wu, R. C. Jackson, and M. Freer, 2018: University of Illinois/Oklahoma Optical Array Probe (OAP) processing software, version 3.1.4. Zenodo, https://doi.org/10.5281/zenodo.1285969.

McMurdie, L. A., and Coauthors, 2022: Chasing snowstorms: The investigation of microphysics and precipitation for Atlantic Coast-Threatening Snowstorms (IMPACTS) campaign. *Bull. Amer. Meteor. Soc.*, **103**, E1243–E1269, https://doi.org/10.1175/BAMS-D-20-0246.1.

Melnikov, V., and J. M. Straka, 2013: Axis ratios and flutter angles of cloud ice particles: Retrievals from radar data. *J. Atmos. Oceanic Technol.*, **30**, 1691–1703, https://doi.org/10.1175/JTECH-D-12-00212.1.

Mitchell, D. L., 1996: Use of mass- and area-dimensional power laws for determining precipitation particle terminal velocities. *J. Atmos. Sci.*, **53**, 1710–1723, https://doi.org/10.1175/1520-0469(1996)053<1710:UOMAAD>2.0.CO;2.

——, R. Zhang, and R. L. Pitter, 1990: Mass-dimensional relationships for ice particles and the influence of riming on snowfall rates. *J. Appl. Meteor. Climatol.*, **29**, 153–163, https://doi.org/10.1175/1520-0450(1990)029<0153:MDRFIP>2.0.CO;2.

Moisseev, D. N., S. Lautaportti, J. Tyynela, and S. Lim, 2015: Dual-polarization radar signatures in snowstorms: Role of snowflake aggregation. *J. Geophys. Res. Atmos.*, **120**, 12 644–12 655, https://doi.org/10.1002/2015JD023884.

Murphy, A. M., A. Ryzhkov, and P. Zhang, 2020: Columnar vertical profiles (CVP) methodology for validating polarimetric retrievals in ice using in situ aircraft measurements. *J. Atmos. Oceanic Technol.*, **37**, 1623–1642, https://doi.org/10.1175/JTECH-D-20-0011.1.

Nguyen, C. M., M. Wolde, and A. Korolev, 2019: Determination of ice water content IWC in tropical convective clouds from X-band dual-polarization airborne radar. *Atmos. Meas. Tech.*, **12**, 5897–5911, https://doi.org/10.5194/amt-12-5897-2019.

Phillips, V. T. J., J.-I. Yano, and A. Khain, 2017: Ice multiplication by breakup in ice–ice collisions. Part I: Theoretical formulation. *J. Atmos. Sci.*, **74**, 1705–1719, https://doi.org/10.1175/JAS-D-16-0224.1.

Reeves, H. D., K. L. Elmore, A. Ryzhkov, T. Schuur, and J. Krause, 2014: Sources of uncertainty in precipitation-type forecasting. *Wea. Forecasting*, **29**, 936–953, https://doi.org/10.1175/WAF-D-14-00007.1.

Ryzhkov, A., and D. Zrnić, 1996: Assessment of rainfall measurement that uses specific differential phase. *J. Appl. Meteor. Climatol.*, **35**, 2080–2090, https://doi.org/10.1175/1520-0450(1996)035<2080:AORMTU>2.0.CO;2.

——, and ——, 1998: Discrimination between rain and snow with a polarimetric radar. *J. Appl. Meteor. Climatol.*, **37**, 1228–1240, https://doi.org/10.1175/1520-0450(1998)037<1228:DBRASW>2.0.CO;2.

——, and ——, 2019: *Radar Polarimetry for Weather Observations*. 1st ed. Springer, 486 pp.

——, ——, and B. A. Gordon, 1998: Polarimetric method for ice water content determination. *J. Appl. Meteor. Climatol.*, **37**, 125–134, https://doi.org/10.1175/1520-0450(1998)037<0125:PMFIWC>2.0.CO;2.

——, ——, J. C. Hubbert, V. N. Bringi, J. Vivekanandan, and E. A. Brandes, 2002: Polarimetric radar observations and interpretation of co-cross-polar correlation coefficients. *J. Atmos. Oceanic Technol.*, **19**, 340–354, https://doi.org/10.1175/1520-0426-19.3.340.

——, M. Pinsky, A. Pokrovsky, and A. Khain, 2011: Polarimetric radar observation operator for a cloud model with spectral microphysics. *J. Appl. Meteor. Climatol.*, **50**, 873–894, https://doi.org/10.1175/2010JAMC2363.1.

Schrom, R. S., 2018: Radar measurements and simulations of ice crystal growth in Arctic mixed phase clouds. Ph.D. thesis, The Pennsylvania State University, 162 pp.

——, and M. R. Kumjian, 2016: Connecting microphysical processes in Colorado winter storms with vertical profiles of radar observations. *J. Appl. Meteor. Climatol.*, **55**, 1771–1787, https://doi.org/10.1175/JAMC-D-15-0338.1.

——, and ——, 2018: Bulk-density representations of branched planar ice crystals: Errors in the polarimetric radar variables. *J. Appl. Meteor. Climatol.*, **57**, 333–346, https://doi.org/10.1175/JAMC-D-17-0114.1.

——, ——, and Y. Lu, 2015: Polarimetric radar signatures of dendritic growth zones within Colorado winter storms. *J. Appl. Meteor. Climatol.*, **54**, 2365–2388, https://doi.org/10.1175/JAMC-D-15-0004.1.

Sinclair, V. A., D. Moisseev, and A. von Lerber, 2016: How dual-polarization radar observations can be used to verify model representation of secondary ice. *J. Geophys. Res. Atmos.*, **121**, 10 954–10 970, https://doi.org/10.1002/2016JD025381.

Smith, T. M., and Coauthors, 2016: Multi-radar multi-sensor (MRMS) severe weather and aviation products: Initial operating capabilities. *Bull. Amer. Meteor. Soc.*, **97**, 1617–1630, https://doi.org/10.1175/BAMS-D-14-00173.1.

Sulia, K. J., J. Y. Harrington, and H. Morrison, 2013: A method for adaptive habit prediction in bulk microphysical models. Part III: Applications and studies within a two-dimensional kinematic model. *J. Atmos. Sci.*, **70**, 3302–3320, https://doi.org/10.1175/JAS-D-12-0316.1.

Thompson, E. J., S. A. Rutledge, B. Dolan, V. Chandrasekar, and B. L. Cheong, 2014: A dual-polarization radar hydrometeor classification algorithm for winter precipitation. *J. Atmos. Oceanic Technol.*, **31**, 1457–1481, https://doi.org/10.1175/JTECH-D-13-00119.1.

Tiira, J., D. N. Moisseev, A. von Lerber, D. Ori, A. Tokay, L. F. Bliven, and W. Petersen, 2016: Ensemble mean density and its connection to other microphysical properties of falling snow as observed in southern Finland. *Atmos. Meas. Tech.*, **9**, 4825–4841, https://doi.org/10.5194/amt-9-4825-2016.

Um, J., G. M. McFarquhar, Y. P. Hong, S.-S. Lee, C. H. Jung, R. P. Lawson, and Q. Mo, 2015: Dimensions and aspect ratios of natural ice crystals. *Atmos. Chem. Phys.*, **15**, 3933–3956, https://doi.org/10.5194/acp-15-3933-2015.

Vardiman, L., 1978: The generation of secondary ice particles in clouds by crystal–crystal collision. *J. Atmos. Sci.*, **35**, 2168–2180, https://doi.org/10.1175/1520-0469(1978)035<2168:TGOSIP>2.0.CO;2.

Welzl, E., 1991: Smallest enclosing disks (balls and ellipsoids). *New Results and New Trends in Computer Science*, H. Maurer, Ed., Lecture Notes in Computer Science, Vol. 555, Springer, 359–370.

Westbrook, C. D., 2014: Rayleigh scattering by hexagonal ice crystals and the interpretation of dual-polarisation radar measurements. *Quart. J. Roy. Meteor. Soc.*, **140B**, 2090–2096, https://doi.org/10.1002/qj.2262.

Wu, W., and G. M. McFarquhar, 2016: On the impacts of different definitions of maximum dimension for nonspherical particles recorded by 2D imaging probes. *J. Atmos. Oceanic Technol.*, **33**, 1057–1072, https://doi.org/10.1175/JTECH-D-15-0177.1.

Zhang, J., and Coauthors, 2016: Multi-Radar Multi-Sensor (MRMS) quantitative precipitation estimation: Initial operating capabilities. *Bull. Amer. Meteor. Soc.*, **97**, 621–638, https://doi.org/10.1175/BAMS-D-14-00174.1.